

## RESEARCH ARTICLE

10.1029/2019JB018221

Enhancing Tsunami Warning Using  $P$  Wave CodaThorne Lay<sup>1</sup> , Chengli Liu<sup>1,2</sup> , and Hiroo Kanamori<sup>3</sup> 

## Key Points:

- Teleseismic  $P_{\text{coda}}$  amplitude generated by water reverberations ( $pwP$ ) increases relative to the direct  $P$  for shallow slip under deep water
- Measurement of high or low  $P_{\text{coda}}/P$  ratios in the distance range from  $30^\circ$  to  $80^\circ$  can reliably identify events with or without shallow slip
- Tsunami warning for subduction zone thrust earthquakes can be improved by rapidly measuring  $P_{\text{coda}}$  to constrain the updip extent of slip

## Supporting Information:

- Supporting Information S1
- Figure Bundle S1
- Figure Bundle S2

## Correspondence to:

T. Lay,  
tlay@ucsc.edu

## Citation:

Lay, T., Liu, C., & Kanamori, H. (2019). Enhancing tsunami warning using  $P$  wave coda. *Journal of Geophysical Research: Solid Earth*, 124, 10,583–10,609. <https://doi.org/10.1029/2019JB018221>

Received 25 JUN 2019

Accepted 12 SEP 2019

Accepted article online 15 SEP 2019

Published online 31 OCT 2019

<sup>1</sup>Department of Earth and Planetary Sciences, University of California, Santa Cruz, CA, USA, <sup>2</sup>Hubei Subsurface Multi-Scale Imaging Key Laboratory, Institute of Geophysics and Geomatics, China University of Geosciences, Wuhan, China, <sup>3</sup>Seismological Laboratory, California Institute of Technology, Pasadena, CA, USA

**Abstract** Most large tsunamis are generated by earthquakes on offshore plate boundary megathrusts. The primary factors influencing tsunami excitation are the seismic moment, faulting geometry, and depth of the faulting. Efforts to provide rapid tsunami warning have emphasized seismic and geodetic methods for quickly determining the event size and faulting geometry. It remains difficult to evaluate the updip extent of rupture, which has significant impact on tsunami excitation. Teleseismic  $P$  waves can constrain this issue; slip under deep water generates strong  $pwP$  water reverberations that persist as ringing  $P_{\text{coda}}$  after the direct  $P$  phases from the faulting have arrived. Event-averaged  $P_{\text{coda}}/P$  amplitude measures at large epicentral distances ( $>80^\circ$ ), tuned to the dominant periods of deep water  $pwP$  ( $\sim 12\text{--}15$  s), correlate well with independent models of whether slip extends to near the trench or not. Data at closer ranges ( $30^\circ$  to  $80^\circ$ ) reduce the time lag needed for inferring the updip extent of rupture to  $<15$  min. Arrival of  $PP$  and  $PPP$  phases contaminates closer distance  $P_{\text{coda}}$  measures, but this can be suppressed by azimuthal or distance binning of the measures. Narrowband spectral ratio measures and differential magnitude measures of  $P_{\text{coda}}$  and direct  $P$  ( $m_B$ ) perform comparably to broader band root-mean-square (RMS) measures.  $P_{\text{coda}}/P$  levels for large nonmegathrust events are also documented. Rapid measurement of  $P_{\text{coda}}/P$  metrics after a large earthquake can supplement quick moment tensor determinations to enhance tsunami warnings; observation of large  $P_{\text{coda}}$  levels indicates that shallow submarine rupture occurred and larger than typical tsunami (for given  $M_W$ ) can be expected.

## 1. Introduction

Large tsunamis have been responsible for great loss of life over time, including recent catastrophic events such as the 2004 Sumatra-Andaman earthquake (e.g., Shearer & Bürgmann, 2010) and the 2011 Tohoku earthquake (e.g., Lay, 2018), along with numerous other events (e.g., Lorito et al., 2016). Mitigation of loss of life requires rapid tsunami warning and evacuation of both local and remote regions based on quick quantification of the earthquake process and resulting tsunami excitation. Good progress has been made in developing seismological approaches (e.g., Duputel et al., 2011; Guilhem et al., 2013; Hirshorn et al., 2013; Kanamori & Rivera, 2008) and geodetic or seismogeodetic approaches (e.g., Blewitt et al., 2006; Colombelli et al., 2013; Hoechner et al., 2013; Melgar & Bock, 2013; Melgar et al., 2013, 2015, 2016; Wright et al., 2012) that can provide rapid assessment of the seismic moment tensor (seismic moment and fault orientation) and/or constraints on the fault slip magnitude and along-coast extent. This information supplements direct tsunami observation by ocean bottom pressure sensors operated by the National Oceanic and Atmospheric Administration (<https://www.tsunami.noaa.gov>) as part of the Pacific tsunami warning system (e.g., Bernard & Titov, 2015) along with an increasing number of seafloor pressure sensors (e.g., Kanazawa et al., 2016; Tanioka, 2018) and seafloor geodetic systems (e.g., Hannemann et al., 2016; Sathiakumar et al., 2016) being operated by other countries.

In recent years, very successful warning of tsunami amplitudes at distant sites has been achieved, as there is sufficient time for analysis of seismic, geodetic, and nearby ocean bottom pressure sensor data to robustly characterize the tsunami wavefield as it expands into the ocean (e.g., Bernard & Titov, 2015; Yamazaki et al., 2012). It remains very challenging to quantify the tsunami excitation rapidly for regional warning, which requires rapid determination of the faulting geometry, seismic moment, slip distribution along the fault, and updip limit of faulting. Figure 1 compares regional maximum tsunami water height measurements (National Oceanic and Atmospheric Administration, [https://www.ngdc.noaa.gov/hazard/tsu\\_db.shtml](https://www.ngdc.noaa.gov/hazard/tsu_db.shtml)) with moment magnitude  $M_W$  for 52 large interplate thrust events (Table 1) that are considered in this

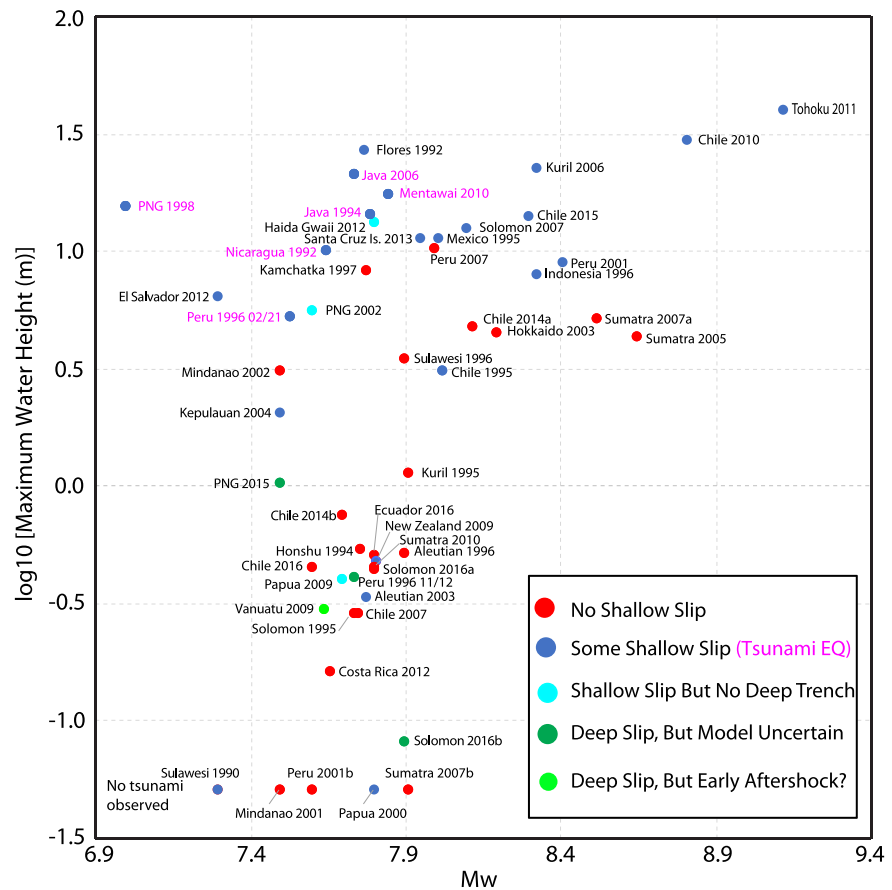


**Figure 1.**  $\log_{10}$  of the maximum water height reported by the National Oceanic and Atmospheric Administration (Table 1) versus  $M_W$  for the 52 interplate thrust events considered in this study. The peak tsunami amplitude or peak runup is used to define maximum water height. No tsunami was reported for the five events located at the bottom. The data are color coded by independent estimates of whether the rupture has at least some slip at shallow depth on the megathrust or not (Table 1).

paper. The maximum water height measurements are a complex mixture of local runup, tide gauge, and deep water pressure sensor observations, so they are only a first-order characterization of the tsunami for each event. The data show systematic increase in tsunami amplitude with  $M_W$  overall, with all events larger than  $M_W$  8.0 generating significant tsunamis. However, there is large variation of maximum water height for magnitudes  $M_W < 8.0$ . In part, this variation can be attributed to variation in rupture depth, with the symbols in Figure 1 being color coded to indicate whether there is evidence from finite-fault inversions (e.g., Hayes, 2017; Ye et al., 2016) for at least some shallow coseismic slip on the megathrust or not (Table 1). The influence of rupture depth is further demonstrated in Figure 2, which plots the same maximum water height measurements as a function of the centroid of the slip distribution for the finite-fault inversions for the thrust events (Table 1). Earthquakes with slip distribution centroid depths less than 20 km tend to generate large tsunamis; these events span a large range of  $M_W$  and include great ruptures like the 2011 Tohoku ( $M_W$  9.1) event and moderate magnitude ( $M_W \sim 7.5\text{--}7.9$ ) tsunami earthquakes (e.g., Kanamori, 1972) highlighted in magenta. Slip under deep water near the trench can be particularly tsunamigenic because large displacements can occur in low rigidity material near the toe of the upper plate. This holds true whether the subduction zone is filled with sediment or is an erosional zone (e.g., Ranero & von Huene, 2000; Scholl & von Huene, 2009). Thus, rapidly determining the depth extent of rupture is important for regional tsunami warning.

Rapid seismic and geodetic data processing can provide critical information about the geometry and strength of the earthquake if sufficient real-time data in the region are available, but these data have limited

**Table 1**

List of Events Used in This Study, Indicating Location, Magnitude, Origin Time, Slip Centroid Depth, and Designation of the Presence of Shallow Slip or Not

Interplate thrust earthquakes									
Date	Location	M <sub>W</sub>	Lat (°)	Lon (°)	Origin time	H <sub>c</sub> (km)	Shallow slip	Maximum water height	NOAA ID # reference
18 Apr. 1990	Sulawesi	7.3	1.19	122.86	13:39:19.0	21.7	Yes	NA	
2 Sep. 1992	Nicaragua	7.7	11.74	-87.34	00:16:01.7	12.4	Yes	9.90 m	2213
12 Dec. 1992	Flores	7.8	-8.48	121.90	05:29:26.4	17.4	Yes	26.2 m	2214
2 June 1994	Java	7.8	-10.48	112.84	18:17:34.0	15.4	Yes	13.9 m	2227
28 Dec. 1994	Honshu	7.8	40.53	143.42	12:19:23.0	27.6	No	0.53 m	2235
30 July 1995	Chile	7.9	-23.34	-70.29	05:11:23.6	37.0	Yes	3.0 m	2249
16 Aug. 1995	Solomon Islands	7.7	-5.80	154.18	10:27:28.6	45.4	No	0.28 m	2250
9 Oct. 1995	Mexico	8.0	19.05	-104.21	15:35:53.9	15.5	Yes	11.0 m	2252
3 Dec. 1995	Kuril	7.9	44.66	149.30	18:01:09.0	25.5	No	1.1 m	2257
1 Jan. 1996	Sulawesi	7.9	0.73	119.93	08:05:10.8	19.8	No	3.43 m	2259
17 Feb. 1996	Indonesia	7.8	-0.89	136.95	05:59:30.6	14.9	Yes	7.7 m	2260
21 Feb. 1996	Peru	7.5	-9.95	-79.59	12:51:01.3	13.6	Yes	5.1 m	2261
10 June 1996	Aleutian Islands	7.9	51.56	-177.63	04:03:35.4	21.7	No	0.51 m	2263
12 Nov. 1996	Peru	7.7	-14.99	-75.68	16:59:44.0	34.2	No?	0.4 m	2269
5 Dec. 1997	Kamchatka	7.8	54.84	162.04	11:26:54.7	42.8	No	8.0 m	2277
17 July 1998	Papua New Guinea	7.0	-2.96	141.93	08:49:13.3	15.3	Yes	15.03 m	2281
17 Nov. 2000	New Britain, PNG	7.8	-5.50	151.78	21:01:56.5	16.1	Yes	NA	
1 Jan. 2001	Mindanao	7.5	6.90	126.58	06:57:04.2	44.0 <sup>a</sup>	No	NA	
23 June 2001	Peru	8.4	-16.27	-73.64	20:33:14.1	18.1	Yes	8.8 m	2373
7 July 2001	Peru	7.6	-17.54	-72.01	09:38:43.5	24.8	No	NA	
5 Mar. 2002	Mindanao	7.5	6.03	124.25	21:16:09.1	28.5	No	3.0 m	2394
8 Sep. 2002	Papua New Guinea	7.6	-3.302	142.95	18:44:23.0	18.2	Yes	5.5 m	2398
25 Sep. 2003	Hokkaido	8.2	41.82	143.91	19:50:06.4	28.7	No	4.4 m	2406
17 Nov. 2003	Aleutian Islands	7.8	51.15	178.65	06:43:06.8	24.6	Yes	0.33 m	2429
11 Nov. 2004	Kepulauan	7.5	-8.15	124.87	21:26:41.2	13.4	Yes	2.0 m	3013
26 Dec. 2004	Sumatra	9.1	3.30	95.98	00:58:53.5	29.0 <sup>a</sup>	Yes?	50.9 m	2439
28 Mar. 2005	Sumatra	8.7	2.09	97.11	16:09:36.5	28.3	No	4.2 m	2487
17 July 2006	Java	7.7	-9.28	107.42	08:19:26.7	11.9	Yes	20.9 m	2832
15 Nov. 2006	Kuril Islands	8.3	46.59	153.27	11:14:13.6	15.0	Yes	21.90 m	3016
1 Apr. 2007	Solomon Islands	8.1	-8.47	157.04	20:39:58.7	14.8	Yes	12.1 m	3037
15 Aug. 2007	Peru	8.0	-13.39	-76.60	23:40:57.9	29.4	No	10.05 m	3168
12 Sep. 2007	Sumatra	8.5	-4.44	101.37	11:10:26.8	30.9	No	5.0 m	3228
12 Sep. 2007	Sumatra	7.9	-2.63	100.84	23:49:03.7	34.1	No	NA	
14 Nov. 2007	Chile	7.8	-22.25	-69.89	15:40:50.5	36.7	No	0.28 m	3293
3 Jan. 2009	Papua	7.7	-0.414	132.89	19:43:50.7	14.2	Yes	0.39 m	3647
15 July 2009	New Zealand	7.8	-45.76	166.56	09:22:29.0	17.6	Yes	0.47 m	4376
7 Oct. 2009	Vanuatu	7.6	-13.01	166.51	22:03:14.5	35.4	No	0.29 m	4442
27 Feb. 2010	Chile	8.8	-36.12	-72.90	06:34:11.5	28.3	Yes	29.0 m	4682
6 Apr. 2010	Sumatra	7.8	2.38	97.05	22:15:01.6	29.1	No	0.44 m	4763
25 Oct. 2010	Mentawai	7.9	-3.49	100.08	14:42:22.5	12.3	Yes	16.9 m	5342
11 Mar. 2011	Tohoku	9.1	38.30	142.37	05:46:24.1	16.1	Yes	38.9 m	10814
27 Aug. 2012	El Salvador	7.3	12.14	-88.59	04:37:13.1	10.5	Yes	6.3 m	5462
5 Sep. 2012	Costa Rica	7.7	10.09	-85.32	14:42:07.8	22.3	No	0.16 m	5464
28 Oct. 2012	Haida Gwaii	7.8	52.79	-132.10	03:04:08.8	8.8	Yes	12.98 m	5467
6 Feb. 2013	Santa Cruz Islands	8.0	-10.80	165.11	01:12:25.8	16.6	Yes	11.0 m	2013
1 Apr. 2014	Chile	8.1	-19.61	-70.77	23:46:47.3	27.5	No	4.63 m	5557
3 Apr. 2014	Chile	7.7	-20.57	-70.48	02:43:13.1	31.7	No	0.74 m	5558
5 May 2015	New Britain, PNG	7.5	-5.46	151.88	01:44:06.4	39.0	Yes?	1.0 m	5583
16 Sept. 2015	Chile	8.3	-31.57	-71.67	22:54:32.9	16.2	Yes	13.6 m	5590
16 Apr. 2016	Ecuador	7.8	0.38	-79.92	23:58:37.0	24.1	No	0.5 m	5599
8 Dec. 2016	Solomon Islands	7.8	-10.68	161.33	17:38:46.3	46.0 <sup>a</sup>	No	0.43 m	5630
17 Dec. 2016	Solomon Islands	7.9	-4.51	153.52	10:51:10.5	53.0 <sup>a</sup>	Yes?	0.08 m	5636
25 Dec. 2016	Chile	7.6	-43.41	-73.94	14:22:27.0	33.0 <sup>a</sup>	No	0.44 m	5637
Outer rise compressional									
19 Mar. 2009	Tonga	7.6	-23.04	-174.66	18:17:40.5	50.6	No	0.15 m	4312
31 Aug. 2012	Philippines	7.6	10.81	126.64	12:47:33.4	37.0	No	0.15 m	5463

Table 1 (continued)

Interplate thrust earthquakes									
Date	Location	M <sub>W</sub>	Lat (°)	Lon (°)	Origin time	H <sub>c</sub> (km)	Shallow slip	Maximum water height	NOAA ID # reference
Intraslab compressional									
8 Aug. 1993	Guam	7.8	12.98	144.80	08:34:24.9	59.0 <sup>a</sup>	No	2.4 m	2221
4 Oct. 1994	Kuril	8.3	43.77	147.32	13:22:55.8	68.0 <sup>a</sup>	No	10.4 m	2230
21 Apr. 1997	Vanuatu	7.7	-12.58	166.68	12:02:26.4	51.0 <sup>a</sup>	No	3.0 m	2273
4 June 2000	Sumatra	7.9	-4.72	102.1	16:28:26.2	44.0 <sup>a</sup>	No	No tsunami	UNDAC (2000)
3 May 2006	Tonga	8.0	-20.19	-174.12	15:26:40.3	62.1	No	0.27 m	2749
Back-arc compressional									
12 July 1993	Hokkaido	7.7	42.85	139.20	13:17:12.0	16.0 <sup>a</sup>	Yes	32.0 m	2219
26 Nov. 1999	Vanuatu	7.5	-16.42	168.21	13:21:15.6	15.0 <sup>a</sup>	Yes	6.6 m	2339
Continental thrusts									
26 Jan. 2001	Gujurat, India	7.7	23.42	70.24	03:16:40.5	20.0 <sup>a</sup>	No	NA	
8 Oct. 2005	Pakistan	7.6	34.54	73.59	03:50:40.8	12.0 <sup>a</sup>	Yes	NA	
20 Apr. 2006	Koryakskiy, Siberia	7.6	60.95	167.09	23:25:02.2	12.0 <sup>a</sup>	Yes	NA	
12 May 2008	Wenchuan, China	7.9	31.00	103.32	06:28:01.5	13.0 <sup>a</sup>	Yes	NA	
25 Apr. 2015	Gorka, Nepal	7.8	28.23	84.73	06:11:26.0	10.5	Yes	NA	
25 Feb. 2018	Papua New Guinea	7.5	-6.07	142.75	17:44:44.1	12.0 <sup>a</sup>	Yes	NA	
Outer rise extensional									
16 May 1995	Loyalty Islands	7.7	-23.01	169.90	20:12:44.2	25.0 <sup>a</sup>	Yes?	0.5 m	2246
13 Jan. 2007	Kuril Islands	8.1	46.24	154.52	04:23:21.2	12.0 <sup>a</sup>	Yes	0.4 m	3019
29 Sep. 2009	Samoa	8.1	-15.49	-172.10	17:48:11.0	12.0 <sup>a</sup>	Yes	22.35 m	4312
6 July 2011	Kermadec	7.6	-29.54	-176.34	19:03:18.3	16.0	Yes	1.2 m	5430
Intraslab extensional									
13 Jan. 2001	El Salvador	7.7	13.05	-88.66	17:33:32.4	56.0 <sup>a</sup>	No	0.25 m	5444
8 Sep. 2017	Chiapas	8.2	15.02	-93.90	04:49:19.2	53.0	No	2.7 m	5658
Oceanic strike slip									
25 Mar. 1998	Balleney	8.1	-62.88	149.53	03:12:25.1	29.0 <sup>a</sup>	Yes?	0.01 m	2587
29 Nov. 1998	Molucca	7.7	-2.07	124.89	14:10:32.0	16.0 <sup>a</sup>	Yes	2.75 m	2588
18 June 2000	Wharton Basin	7.9	-13.80	97.45	14:44:13.3	15.0 <sup>a</sup>	Yes	0.3 m	2341
16 Nov. 2000	New Ireland, PNG	8.0	-3.98	152.17	04:54:56.7	24.0 <sup>a</sup>	Yes?	3 m	2281
23 Dec. 2004	Macquarie	8.1	-49.31	161.34	14:59:04.4	27.0 <sup>a</sup>	Yes	0.3 m	3014
11 Apr. 2012	Wharton Basin	8.6	2.33	93.06	08:38:36.7	46.0 <sup>a</sup>	Yes	0.82 m	Wang et al. (2012)
11 Apr. 2012	Wharton Basin	8.2	0.80	92.46	10:43:10.9	55.0 <sup>a</sup>	Yes?	Not significant	Wang et al. (2012)
17 Nov. 2013	Scotia Ridge	7.8	-60.27	-46.40	09:04:55.5	24.0 <sup>a</sup>	Yes	0.15 m	5534
2 Mar. 2016	Wharton Basin	7.8	-4.59	94.33	12:49:48.1	18.4	Yes	0.21 m	5598
17 July 2017	Komandorsky	7.8	54.44	168.86	23:34:13.7	16.7	Yes	0.1 m	5654
23 Jan. 2018	Gulf of Alaska	7.8	56.00	-149.17	09:31:40.9	21.0	Yes	0.25 m	5673
Continental strike slip									
14 Nov. 2001	Kunlun, Tibet	7.8	35.95	90.54	09:26:10.0	15.0 <sup>a</sup>	Yes	NA	
3 Nov. 2002	Denali, Alaska	7.9	63.51	-147.45	22:12:41.5	15.0 <sup>a</sup>	Yes	NA	

Note. Events are grouped by mechanism type and tectonic environment. Maximum water height reported by the National Oceanic and Atmospheric Administration (NOAA) (NA denotes not available) and the NOAA ID number are indicated for each event. NOAA ID is from NGDC/WDS Tsunami Event Database (<https://www.ngdc.noaa.gov/nndc/struts/form?t=101650&s=72&d=i67>). PNG = Papua New Guinea; UNDAC = United Nations Disaster Assessment and Coordination.

<sup>a</sup>H<sub>c</sub> is global centroid moment tensor depth; otherwise it is mean slip depth from finite-fault inversion (e.g., Ye et al., 2016).

resolution of the far-offshore (updip) extent of thrust faulting, even for very well instrumented areas (e.g., Lay, 2018). Centroids of long-period moment tensors determined from regional data that lack good azimuthal distribution and ground displacements detected by one-sided onshore GPS generally do not constrain the updip limit of slip. Radiated near-field and teleseismic *P* wave energy allows shallow-rupturing tsunami earthquakes to be recognized by deficiency of their high-frequency radiation (e.g.,

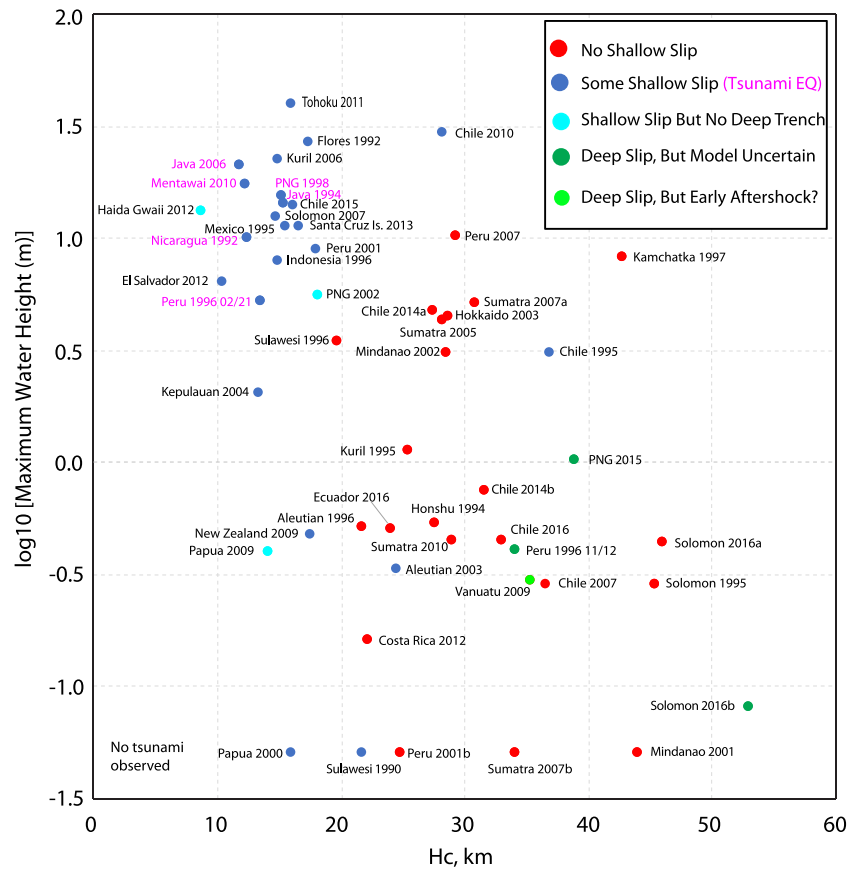


**Figure 2.**  $\log_{10}$  of the maximum water height reported by the National Oceanic and Atmospheric Administration versus  $H_c$ , the centroid of the slip distribution for the finite-faults reported in Table 1 for the 52 interplate thrust events considered in this study. No tsunami was reported for the five events located at the bottom. The data are color coded as in Figure 1.

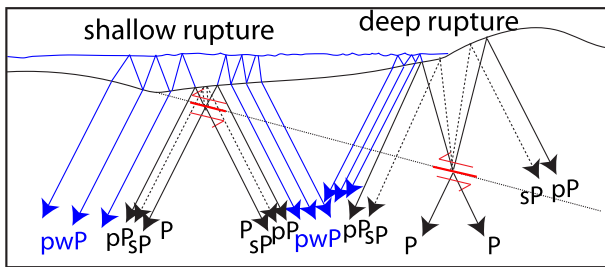


**Figure 3.** Schematic raypaths for teleseismic  $P$  phases generated by thrust faulting earthquakes at different depths on subduction zone plate boundary megathrust faults. Both shallow and deep thrust events will produce direct  $P$  and surface reflected  $pP$  and  $sP$  phases (black lines and dots) at all teleseismic distances. Shallow slip, below the toe of the accretionary prism, will also generate leaky acoustic wave reverberations in the water, comprising the  $pwP$  series (blue), with the time between arrivals being larger for deeper water. Deep slip will not produce  $pwP$  for stations at landward azimuths and will produce relatively high-frequency  $pwP$  at seaward azimuths. The coda ringing produced by  $pwP$  can thus indicate whether an interplate thrust has significant slip at shallow depth under deep water or not. This information can guide rapid assessment of the likely strength of tsunami generated by a large megathrust rupture.

Newman & Okal, 1998; Sahakian et al., 2019; Ye et al., 2013), as does comparison of short-period  $P$  wave magnitude and long-period moment magnitude,  $M_W$  (e.g., Kanamori & Ross, 2019). However, some ruptures, like the 2011 Tohoku earthquake, involve slip across the entire seismogenic plate boundary width (Lay, 2018), complicating such approaches. If the occurrence of shallow slip in part, or all, of the rupture can be determined reliably, regional tsunami warnings can be enhanced in terms of recognizing the potential for a larger-than-normal tsunami to have been excited by slip extending out to near the trench. This study presents a strategy by which that can be done in a time frame of <15 min, which can help on regional tsunami amplitude warning.

The approach presented here builds upon an initial study by Lay and Rhode (2019), which introduced the concept of using the strength of teleseismic  $P_{\text{coda}}$  relative to  $P$  as a proxy for the occurrence of some slip or no slip at shallow depth under deep water for large megathrust ruptures. That work follows on early studies of  $P_{\text{coda}}$  generation for submarine faulting (e.g., Ihmlé & Madariaga, 1996; Ward, 1979; Wiens, 1987, 1989). The underlying idea is simple and is illustrated in Figure 3. For thrust faulting on dipping plate boundary megathrusts in either island arc or continental arc subduction zones, earthquakes radiate both downgoing  $P$  and upgoing  $P$  and  $S$  that will reflect off the rock surface as depth phases  $pP$  and  $sP$ , respectively. For upgoing  $P$  paths that reach the rock surface under

water, some energy transmits into the water as acoustic waves that will reflect off the water surface and travel back down to the seafloor where some energy transmits into the rock as the phase  $pwP$ , while some reflects back into the water producing a series of leaking reverberations that cause teleseismic  $pwP$  arrivals to “ring” in a sequence of arrivals with time interval controlled by the water depth. For water deeper than 6 km, the period of  $pwP$  oscillations is about 12 to 15 s, with a gradually decaying signal that can persist for many tens of seconds as  $P_{\text{coda}}$  after the direct ( $P+pP+sP$ ) wave packet has completed its ground motions at a teleseismic station. If the source involves at least some slip at shallow depth on the megathrust under deep water near the trench, reverberative  $pwP$  with a period of  $\sim 13$  s will be present in the  $P_{\text{coda}}$  at all azimuths from the source. If the source involves only slip deeper on the megathrust, close to the coast, arcward azimuths will receive little/no  $pwP$  arrivals, while seaward azimuths can have short period ( $<10$  s)  $pwP$  oscillations. Thus, observation of high  $P_{\text{coda}}$  amplitudes relative to  $P$  amplitudes is expected for shallow slip under deep water, with source radiation patterns for thrust events tending to make the ratios highest in the seaward direction because at those azimuths the downgoing  $P$  is more nodal than the upgoing  $pP$  that generates the  $pwP$  series (see synthetic examples in Lay & Rhode, 2019).

Conceptually, one can infer the occurrence or nonoccurrence of shallow slip by simple measures of the signal strength of  $P_{\text{coda}}$  relative to  $P$  for a given event. Essentially, this involves remotely “hearing” prolonged booming echoes of the source sounds when slip occurs under deep water. Lay and Rhode (2019) confirm this expectation for a particular metric of teleseismic  $P_{\text{coda}}/P$  at large epicentral distances ( $>80^\circ$ ), providing a new probe of the updip extent of rupture for megathrust events. Here we extend this approach for the practicalities of rapid tsunami warning, which requires use of data at  $<80^\circ$  distance to reduce the time lag for decision making.

## 2. Data and RMS Methods

Lay & Rhode, 2019 focus on teleseismic  $P$  waves recorded at epicentral distances from  $80+^\circ$  to  $120^\circ$  where there is a several minute-long time interval between the first  $P$  arrival and the arrival of secondary seismic phases such as  $PP$  and  $PKIKP$ . For a large earthquake rupture that radiates direct  $P$  waves for a duration of less than 2 min there is about 2 min of immediately ensuing  $P_{\text{coda}}$  duration in which no other arrival from radial Earth structure is expected. Measures of  $P_{\text{coda}}$  amplitudes relative to  $P$  amplitudes can then reliably assess whether the  $P_{\text{coda}}$  is augmented by persistent  $pwP$  near-source reverberations that indicate rupture under water or just has typical levels of scattered energy from propagation through the heterogeneous 3-D Earth. Summing measures from many stations suppresses effects of individual station/path complexity and enhances sensitivity to energy emerging from the source region. Band-pass filtering the data to emphasize the period range of  $pwP$  expected for rupture under deep water (Lay & Rhode, 2019; use a passband of 7 to 15 s) near the trench increases the sensitivity of the measures to the updip limit of slip during the earthquake as suggested by Figure 3.

Use of large distance  $P$  waves results in significant delay after the earthquake, given that the first  $P$  arrival at  $80^\circ$  will have a travel time of about 12 min, while that at  $120^\circ$  will take about 15 min to reach the station. The duration of the  $P$  wave generated during rupture (composed of all the  $P+pP+sP$  arrivals from the space-time distribution of slip on the megathrust) plus an interval of  $P_{\text{coda}}$  sufficient for stable measurement must be allowed for, giving an effective delay of  $\sim 18+$  min for event-averaged assessment of the relative amplitude of  $P_{\text{coda}}$  to  $P$ . This can certainly contribute to regional and remote tsunami warning but is clearly of limited use for local tsunami warning.  $P$  waves at an epicentral distance of  $30^\circ$  have travel times of about 5 min, so use of signals at closer distances can cut minutes off the contribution to tsunami warning. Even closer distance might be considered, but the strong  $pwP$  ringing involves steep raypaths (small ray parameters) and is more pronounced at teleseismic distances where the  $P$  waves dive steeply into the mantle ( $P_n$  phases have weaker  $pP_n$  signals and hence will have lower  $pwP_n$  amplitudes). Triplications from upper mantle discontinuities add complexity and total duration to direct  $P$  arrivals at distances from  $15^\circ$  to  $30^\circ$ . At close distances, strong  $S$  phases and surface waves may obscure the  $P_{\text{coda}}$  signal as well. Generation of seismic coda observed at distances less than  $30^\circ$  still does warrant further investigation, but here we only consider observations of  $P_{\text{coda}}$  at distances larger than  $30^\circ$ , where direct  $P$  waves are simpler. We seek to reduce the measurement delays to  $<15$  min for contribution to local tsunami warning, which is somewhat longer than the lag time required for stable moment tensor inversions using long-period signals for well-instrumented regions. The

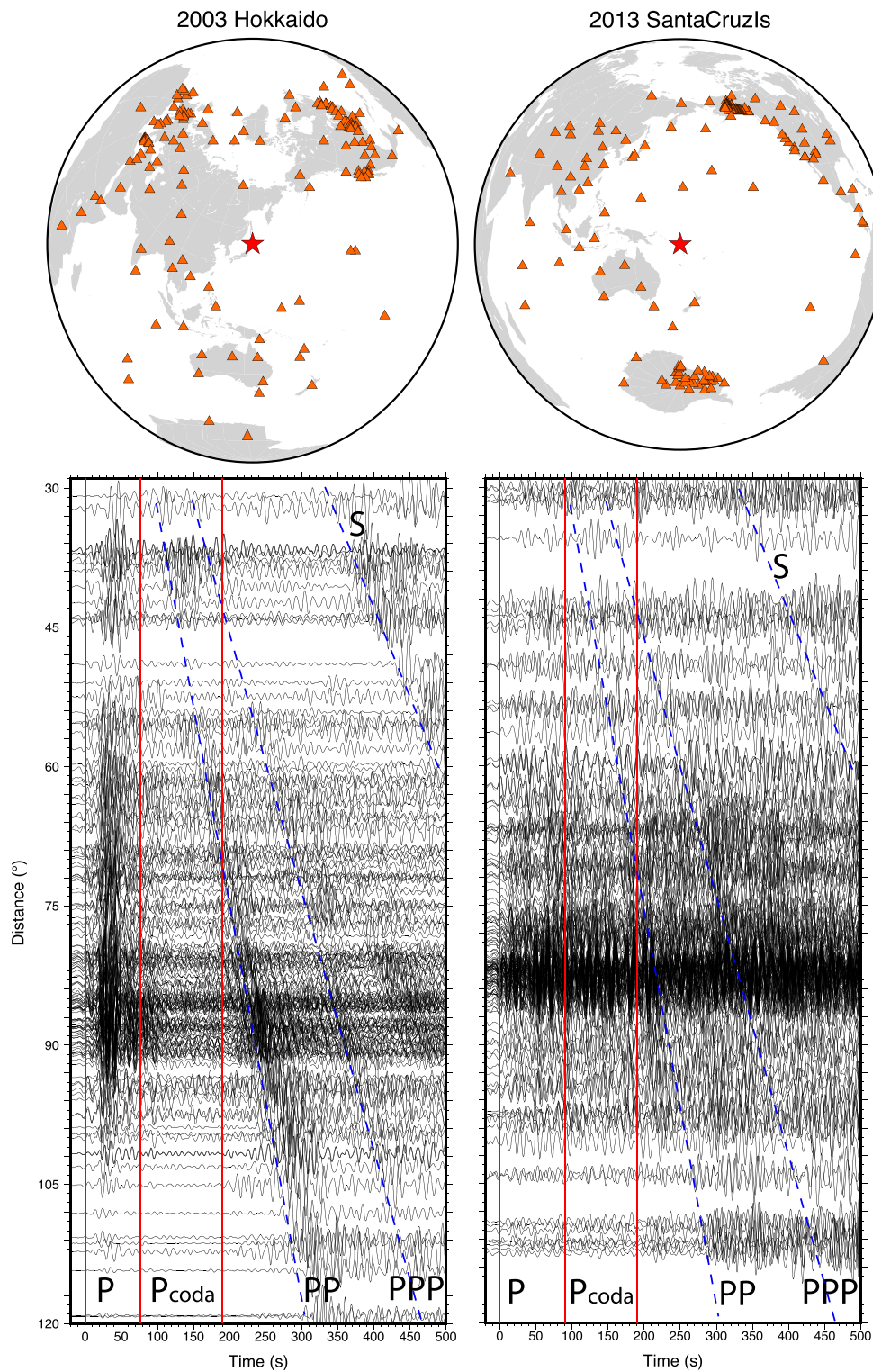


**Figure 4.** Profiles of vertical component ground velocity recordings, Butterworth band-pass filtered in the passband 7–15 s, aligned on the  $P$  wave arrival and plotted as a function of epicentral distance from  $30^\circ$  to  $120^\circ$  for the (left) 25 September 2003 Hokkaido, Japan earthquake ( $M_W$  8.2) and (right) 6 February 2013 Santa Cruz Islands ( $M_W$  8.0) earthquake. The maps (top) show event epicenter (red star) and station distribution (red triangles) for each event. The red lines on the profiles indicate the time intervals for the  $P$  wave signal from the source (first interval) and the  $P_{\text{coda}}$  (second interval). Approximate moveout curves (blue dashed lines) of secondary arrivals  $PP$ ,  $PPP$ , and  $S$  are labeled. High coda levels make these phases difficult to see for the 2013 event. The 2003 event did not have shallow rupture, while the 2013 event did.

added complication of the closer distance range is that secondary phases such as  $PP$ ,  $PPP$ , and  $PcP$  (usually small) cut through the  $P_{\text{coda}}$  time interval as shown in Figure S5 of Lay and Rhode (2019).

Figure 4 shows representative profiles of global seismic  $P$  wave observations, involving ground velocities filtered in the 7- to 15-s period range, plotted over the distance range  $30^\circ$  to  $120^\circ$ . The 2003 Hokkaido earthquake has been shown to not have coseismic slip extending to near the trench (e.g., Miyazaki et al., 2004), while the 2013 Santa Cruz Islands event does have substantial, tsunamigenic slip at shallow depth below deep water (e.g., Lay et al., 2013). The profiles, aligned on the  $P$  wave, have red lines bracketing the interval for the direct  $P$  ( $+pP+sP$ ) ground motions (first interval) as defined by the source duration of the moment rate functions for the earthquakes inferred from finite-fault inversions (Ye et al., 2016), with 20 s added to account for the last depth phase arrivals. The subsequent interval is the  $P_{\text{coda}}$  duration, which was defined in Lay and Rhode (2019) by the time from the end of the  $P$  window to the arrival time of  $PP$  at  $\sim 80^\circ$ . For the 2003 event, clear  $PP$ ,  $PPP$ , and  $S$  phase branches are apparent in the ground velocities, highlighted by dashed blue lines.  $PP$ , in particular, moves through the  $P_{\text{coda}}$  window in the distance range  $30^\circ$  to  $70^\circ$ . For the 2013 event, note that the discrete travel time branches are less apparent at all ranges and the ground motions in the  $P_{\text{coda}}$  window are comparable to those in the  $P$  window, in contrast to the 2003 profile. The azimuthal distributions of global network broadband stations used (GSN, FDSN, and Antarctica BB) are shown in the maps relative to the hypocenters. The azimuthal distributions are nonuniform, and there is an intrinsic tendency for stations at seaward directions to be sparse, while clusters of continental stations occur at landward directions; this motivates an azimuthal binning procedure when generating event-averaged parameters.

The data beyond  $80^\circ$  in Figure 4 are particularly simple to evaluate because the  $P_{\text{coda}}$  levels are not contaminated by expected secondary phases. Measurements for each station, in a given passband, of the ratios of root-mean-square (RMS) amplitudes of  $P_{\text{coda}}$  (for the time window following the  $P$  window up to arrival of the  $PP$  phase at  $80^\circ$ ) to RMS amplitudes of  $P$  (for the time window spanning  $P+pP+sP$  arrivals from source slip), are denoted as  $RMS_{C/P}$ . The mean or median values for the stations in  $10^\circ$  azimuth bins are determined, and the overall mean or median of the binned values is computed. This provides easily obtained event-specific measures sensitive to the presence or absence of strong  $pWP$ . Lay and Rhode (2019) found that event mean  $RMS_{C/P}$  varies by a factor of 4 among 39 major and great subduction zone thrust events.  $RMS_{C/P} > 0.61$  was found for all events (19) with independent finite-fault models indicating at least some slip located at shallow depth on the megathrust below deep ocean, while all events (16) except for two with no indication of shallow slip have  $RMS_{C/P} < 0.61$ . One of the exceptions has a readily recognized early aftershock in the  $P_{\text{coda}}$  window (rather than ringing  $pWP$ ), while the other has a relatively uncertain finite-fault model that is being investigated further. Two events have shallow slip, but lack a nearby deep trench, so they should not have long-period  $pWP$ ; indeed, they have low  $RMS_{C/P}$  values. Computing medians of the  $10^\circ$  azimuthal bins gives similar results with slightly greater separation of the bimodal populations (see Figure S8 in Lay & Rhode, 2019).

The data for the 39 interplate thrust events considered by Lay and Rhode (2019) are augmented here to include broadband observations for the distance range  $30^\circ$  to  $120^\circ$ , and corresponding data for 14 more large megathrust earthquakes from 1990 to 2018 are added (although the 2004 Sumatra  $M_W$  9.2 earthquake is not used for coda measurements due to its extremely long  $P$  duration). For the new events we again draw upon published finite-fault models (e.g., Hayes, 2017; Ye et al., 2016) to constrain the  $P$  wave duration and the bimodal classification as having shallow coseismic slip or not. In addition, corresponding data for 34 large shallow earthquakes in different tectonic environments (outer rise compressional, intraslab compressional, back-arc compressional, continental thrusts, outer rise extensional, intraslab extensional, oceanic strike slip, and continental strike slip) are analyzed. Among the latter, the thrust- and normal-faulting dip-slip events in oceanic environments are also of concern for tsunami warning. Table 1 lists the hypocentral parameters and  $M_W$  of the 87 earthquakes, along with estimates of the centroid depth of the finite-fault slip distributions ( $H_c$ ) and a priori classification of whether or not the event has shallow slip. Figure 5 shows the global centroid moment tensor focal mechanisms for all of the events, color coded to separate the subduction zone megathrust events (blue) from the other categories of events (red). The data set includes all useable shallow events larger than  $M_W$  7.5–

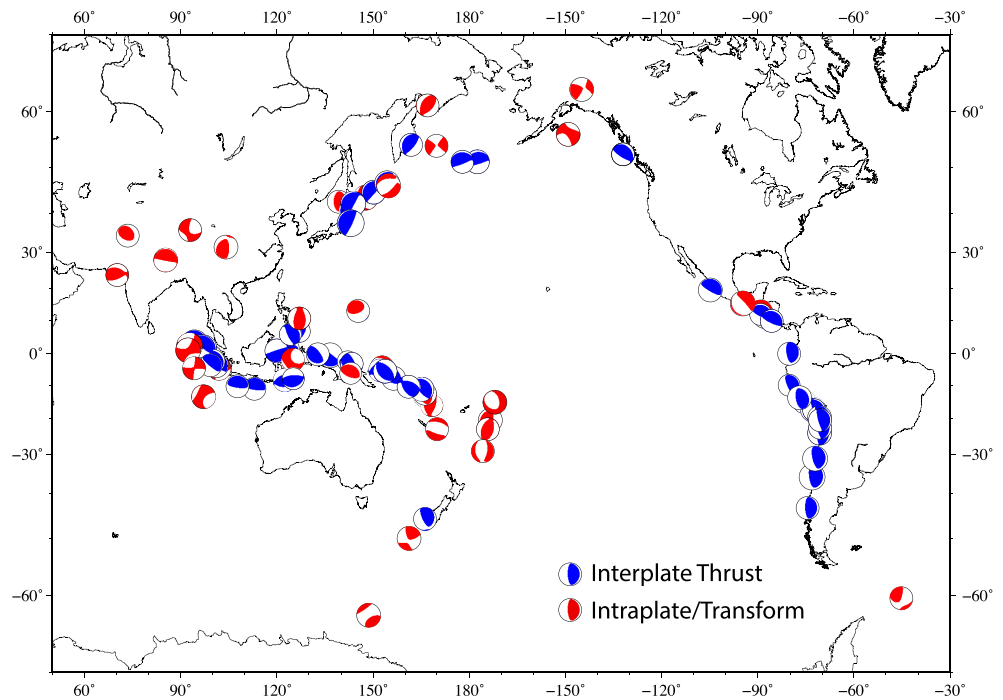


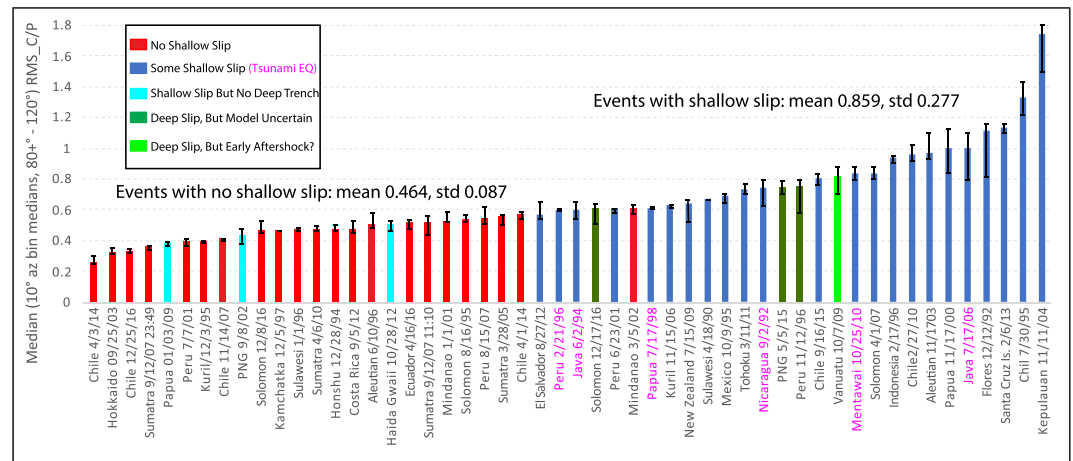
**Figure 5.** Map of 87 major and great shallow (<70 km deep) earthquakes from 1990 to 2016 used in this study showing their lower hemisphere global centroid moment tensor solutions. Mechanisms are color coded for interplate thrust events (blue) and intraplate or strike-slip transform fault events of various faulting geometry (red). Based on examination of published finite-fault models, each interplate thrust event is characterized as either suspected to have some shallow coseismic slip (or entirely shallow coseismic slip for tsunami earthquakes) or suspected to not have significant shallow slip (Figure 6). Specific event information is given in Table 1.

7.6 for all mechanism types from 1990 to 2018 along with a handful of smaller subduction zone megathrust events included to provide a good balance of deep-slip and shallow-slip events with good sampling of the regions that generate most tsunamis. Intrinsically, regions that have experienced few or no recent large earthquakes like Cascadia, Izu, Marianas, and Ryukyus are not well represented.

### 3. RMS Coda Measures for Interplate Thrust Events

Measurements are made for all events following the basic procedure introduced by Lay and Rhode (2019); for each new event the data from 80° to 120° are used to compute the  $RMS_{C/P}$  ratios at all stations using the 7- to 15-s band-pass filtered velocity signals, and these are binned in 10° azimuthal windows. For the binning, we compute the median of the ratios in each bin (rather than average) and then we compute the median of the bin medians to give the final event median  $RMS_{C/P}$  value. For the original 39 events, we use the same data from Lay and Rhode (2019); some of those events had original distance windows of 90° to 120° or 100° to 120° and included all broadband data from temporary deployments yielding many observations. We compute median  $RMS_{C/P}$  using medians of 10° azimuthal bins for the original distance windows to provide reference measurements with continuity to the earlier study (designated with ranges 80+° to 120°), given the near-perfect bimodal separation of the two populations of slip depth it provided. Very small differences are found using all data in the 80° to 120° range from just GSN, FDSN, and Antarctic stations for those 39 events (the respective median  $RMC_{C/P}$  measures have a correlation coefficient  $r = 0.970$ ).

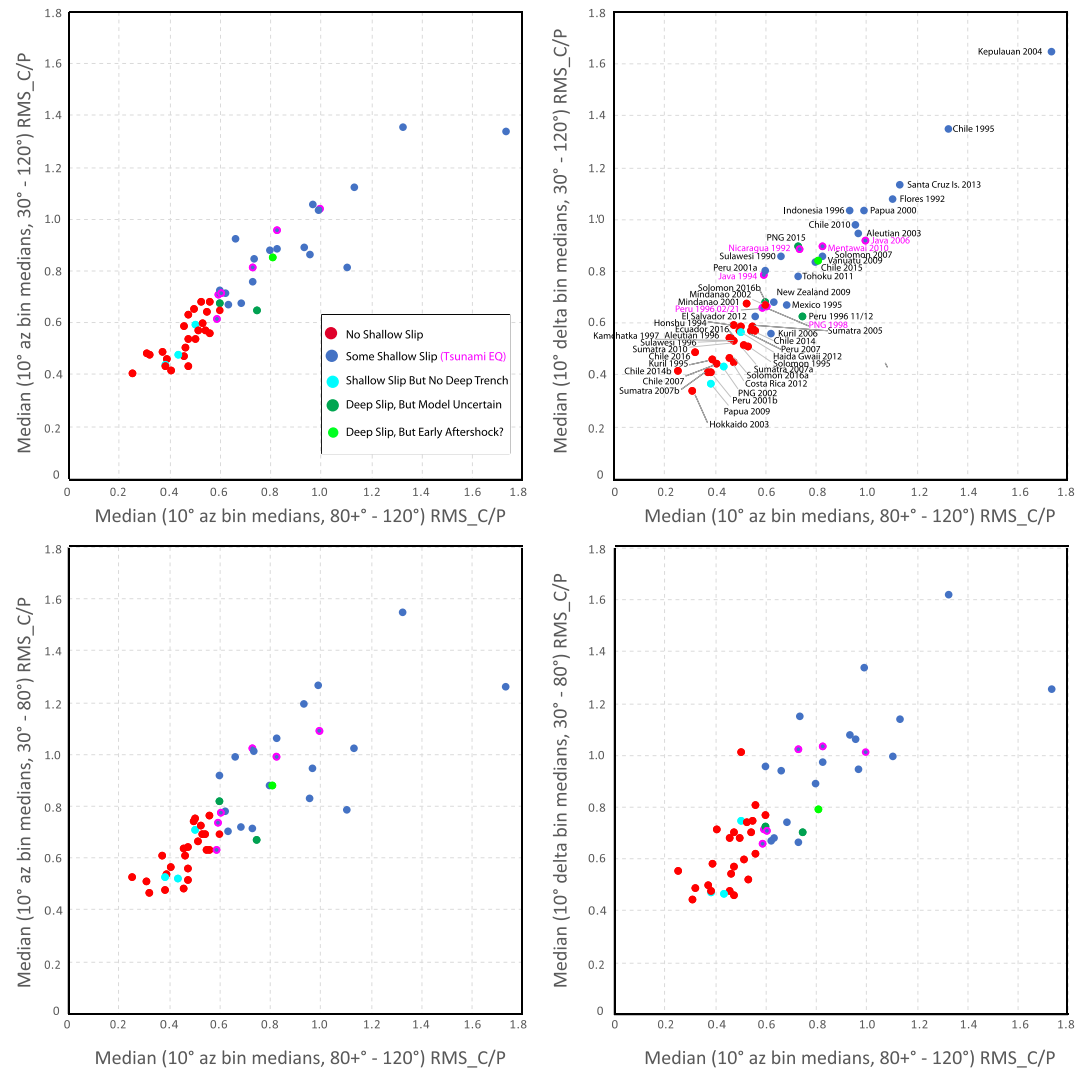
The median  $RMS_{C/P}$  measures for all of the interplate thrust events are plotted in ascending order in Figure 6. The corresponding values are listed in Table S1 in the supporting information. The range of the 40th to 60th percentile measurements for each event is included as an indication of stability of the median values (these bounds generously approximate a standard error of the median for the skewed distributions). Color coding is used to indicate the independent inferences of whether there was at least some shallow slip during the rupture (blue) or not (red). The distribution is very similar to that for the 39 events in Lay and



**Figure 6.** Event median  $RMS\_C/P$  for medians of  $10^\circ$  azimuthal bins for measurements at epicentral distances from  $80^\circ+$  to  $120^\circ$ , ordered by increasing value for the 52 large interplate thrust earthquakes considered in this analysis. Red bars indicate events that are thought to have no shallow slip based on the available slip models, while blue bars are thought to have at least some shallow slip or only shallow slip. Cyan bars indicate events that rupture shallow depths but have no deep water trench. Dark green bars have uncertain slip models but lack shallow slip in published results. The light green bar is for an event with an early aftershock contaminating the coda. The bounds on each measurement indicate the 40th and 60th percentile values. The separate means and standard deviations (std.) of the red and blue populations are shown above the distributions.

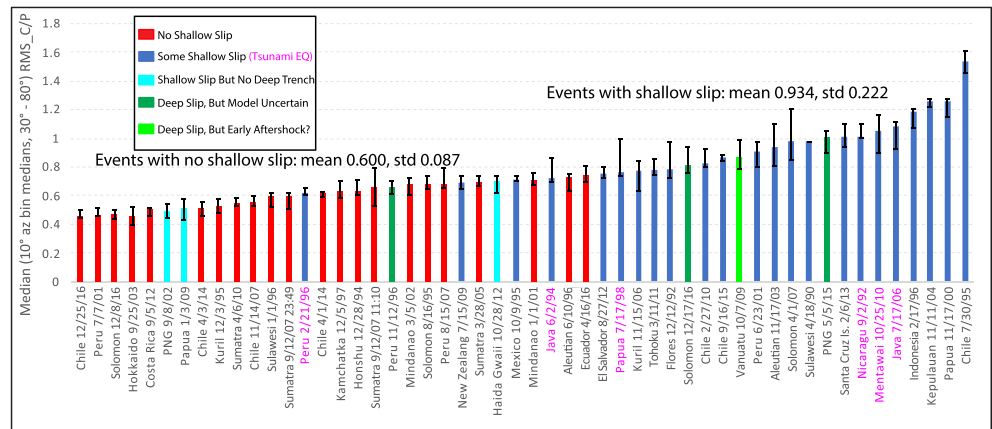
Rhode (2019), with the same outliers, but there are 13 new events and our use of median of bin medians slightly reorders some events. One new event (2002 Papua New Guinea) with shallow slip occurred in a region with no deep trench, giving a total of three such cases (cyan). Two new events have moderately high  $RMS\_C/P$  but uncertain slip models; 17 December 2016 Solomon Islands (e.g., Lay et al., 2017; <https://earthquake.usgs.gov/earthquakes/search/>; Lee et al., 2018) and 5 May 2015 Papua New Guinea (e.g., Ye et al., 2016; <https://earthquake.usgs.gov/earthquakes/search/>), giving three such cases. The two new events involve initially deep ruptures (the 2016 Solomon Islands event likely begins as an intraplate rupture) that propagate or trigger updip, and while the finite-fault models do suggest that some slip may extend to near the trench, the resolution is limited and the amount of shallow slip varies among the finite-fault models. The 2016 Solomon Islands event produced outer rise normal faulting aftershocks along part of the rupture, a common indicator of shallow coseismic slip (e.g., Sladen & Trevisan, 2018; Wetzler et al., 2017), while the 2015 Papua had shallow thrust-faulting aftershocks all the way to the trench (Wetzler et al., 2017). Such events, with relatively deep moment tensor centroid depths, present particular difficulties for tsunami warning. One new event (5 March 2002 Mindanao) does not have evidence for shallow slip in available models (e.g., Ye et al., 2016; <https://earthquake.usgs.gov/earthquakes/search/>) but locates within the population that does, giving one clear outlier to the general separation of the populations that cannot be readily accounted for unless the published finite-fault models are found to be misleading, which is being examined separately.

If we only consider the red values (events with no shallow slip) in Figure 6, the mean value of median  $RMS\_C/P$  for that population is 0.464 with a standard deviation of 0.087. The mean value of the blue  $RMS\_C/P$  values (events with some/all shallow slip under a deep trench) is 0.859 with a standard deviation of 0.277. Observation of correspondingly measured median  $RMS\_C/P$  larger than  $\sim 0.65$  is strongly suggestive of  $pwP$  enhancement of the coda, whereas values less than  $\sim 0.55$  are strongly suggestive of no shallow slip in the rupture. Intermediate values are ambiguous, and this includes some modest size tsunami earthquakes (names highlighted in magenta). There are significant changes in the availability of global seismic data over time; more recent events have substantially larger data sets with more complete azimuthal sampling, so earlier events (pre-2000) tend to have larger uncertainty. Rather than diving into a complex statistical classification effort (the subpopulations means are statistically distinct, but the actual measurements present a continuum rather than a bimodal distribution), we now consider the prospect of achieving comparable first-order population segregation using data at closer distances, as desirable for more rapid tsunami warning application.



**Figure 7.** Comparison of  $RMS_{C/P}$  measures for interplate thrust events made using different distance ranges and data binning. The top row compares median  $RMS_{C/P}$  for data spanning the distance range  $30^\circ$  to  $120^\circ$  using medians of  $10^\circ$  azimuthal bins (left) or  $10^\circ$  distance bins (right) with median  $RMS_{C/P}$  for data spanning the range  $80+^\circ$  to  $120^\circ$  with  $10^\circ$  azimuthal bins. The lower row compares median  $RMS_{C/P}$  for data spanning the distance range  $30^\circ$  to  $80^\circ$  using medians of  $10^\circ$  azimuthal bins (left) or  $10^\circ$  distance bins (right) with median  $RMS_{C/P}$  for data spanning the range  $80+^\circ$  to  $120^\circ$  with  $10^\circ$  azimuthal bins. Color coding corresponds to Figure 1, indicating whether independent evidence indicates the presence of shallow slip with deep water trench (blue), no shallow slip (red), shallow slip with no deep water trench (cyan), deep slip in uncertain solutions (dark green), or occurrence of an early aftershock in the coda window (green).

We used the same  $P$  and  $P_{coda}$  windows to compute  $RMS_{C/P}$  for the data for each event for distance ranges of  $30^\circ$  to  $120^\circ$  and  $30^\circ$  to  $80^\circ$ . The expanded sampling provided by these data allows us to compare  $10^\circ$  azimuthal binning with  $10^\circ$  distance binning in the computation of medians of azimuthally binned or distance-binned medians. Referring to the examples in Figure 4, it is clear that  $10^\circ$  distance binning will lead to  $P_{coda}$  measures at less than  $60^\circ$  being enhanced for events without high coda but only modestly affected for events with high coda. Variation of area covered by distance bins at different ranges is inconsequential given the highly nonuniform distribution of stations. Using  $10^\circ$  azimuth binning will tend to mitigate the effects of  $PP$  contamination at closer distances by computing the median for azimuths with a wide range of distances and prevents dense continental station distributions from being overrepresented and sparse data at seaward directions from being underrepresented. Figure 7 compares the resulting median  $RMS_{C/P}$  values with those for the  $80+^\circ$  to  $120^\circ$  values from



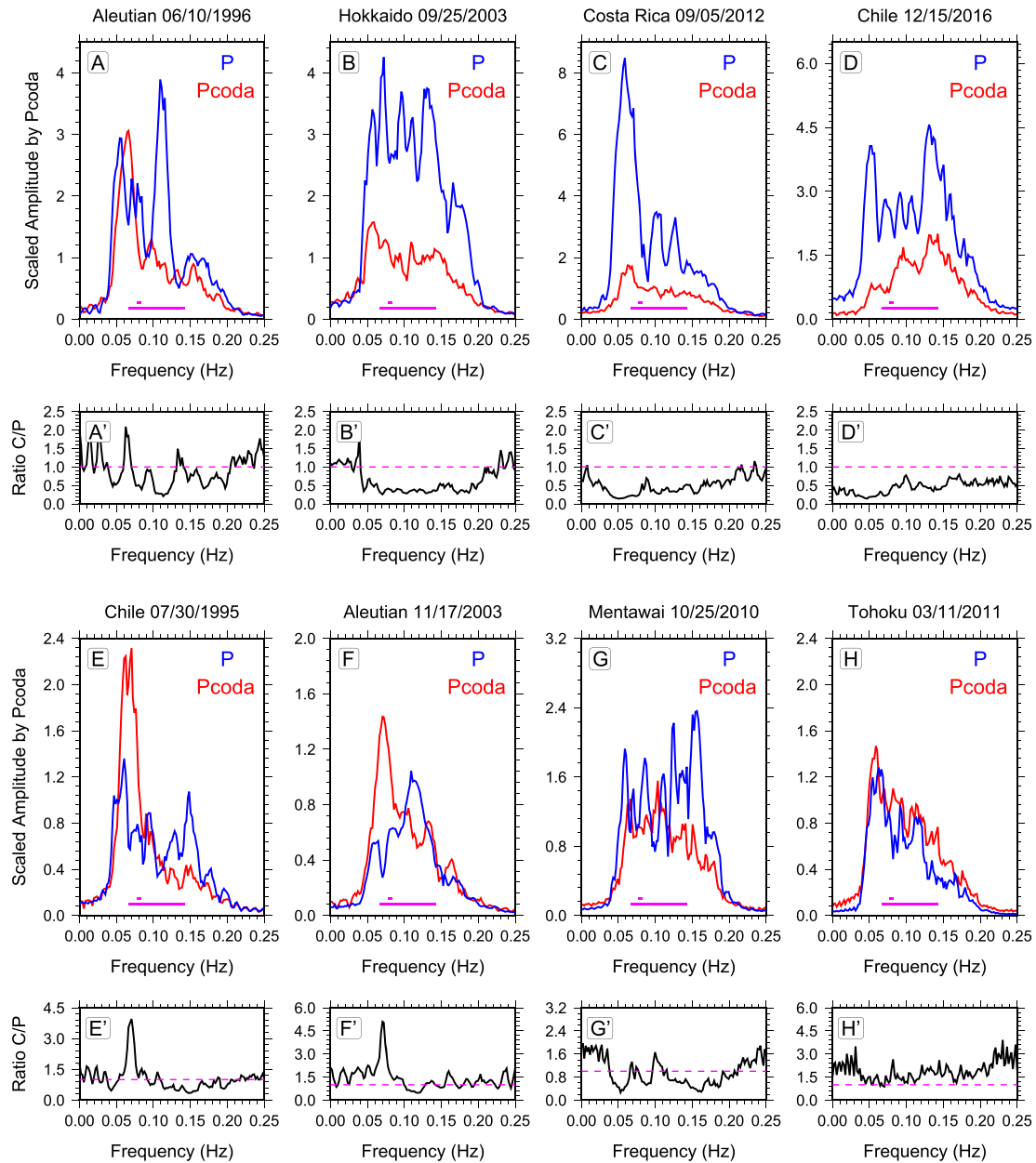
**Figure 8.** Event median  $RMS_{C/P}$  for medians of  $10^\circ$  azimuthal bins for measurements at epicentral distances from  $30^\circ$  to  $80^\circ$ , ordered by increasing value for the 52 large interplate thrust earthquakes considered in this analysis. Red bars indicate events that are thought to have no shallow slip based on the available slip models, while blue bars are thought to have at least some shallow slip or only shallow slip. Cyan bars indicate events that rupture shallow depths but have no deep water trench. Dark green bars have uncertain slip models but lack shallow slip in published results. The light green bar is for an event with an early aftershock contaminating the coda. The bounds on each measurement indicate the 40th and 60th percentile values. The separate mean and standard deviation (std.) of the red and blue populations are shown above the distribution.

Figure 6. The corresponding measurements are all listed in Table S1. The same color coding as used in Figure 6 is used for the comparisons in Figure 7.

There is very strong correlation between the results for the  $30^\circ$  to  $120^\circ$  estimates and the  $80^\circ$  to  $120^\circ$  values for both azimuthal binning ( $r = 0.934$ ) and for distance binning ( $r = 0.966$ ). The data do overlap at large distances although we cull the data set spanning  $30^\circ$  to  $120^\circ$  to remove all non-FDSN networks and transportable station deployments from the original large distance data set of Lay and Rhode (2019). The separation of populations is still very good, but there is more overlap for values around  $0.6$  for the  $30^\circ$  to  $120^\circ$  measures than for the  $80^\circ$  to  $120^\circ$  measures. For the  $30^\circ$  to  $80^\circ$  estimates, increased influence of  $PP$  and  $PPP$  biases in coda amplitudes is expected, with less efficacious suppression by binning. However, the correlations with the  $80^\circ$  to  $120^\circ$  measures are still quite good for both azimuthal binning ( $r = 0.845$ ) and distance binning ( $r = 0.834$ ).

The median  $RMS_{P/C}$  measures for data from  $30^\circ$  to  $80^\circ$  with  $10^\circ$  azimuthal binning are plotted in sorted order in Figure 8, for comparison with Figure 6. There is more mixing of the populations for values around  $0.70 \pm 0.05$  but still very good separation of the populations for larger and smaller values. The Peru 21 February 1996 tsunami earthquake is now an outlier, with low coda level. This early event has very limited data at the closer distances in the seaward direction, so it is dominated by arcward data that lack strong  $pwP$ . The mean value of the red (no shallow slip) median  $RMS_{C/P}$  values in Figure 8 is  $0.600$ , with a standard deviation of  $0.087$ . The mean value of the blue (some/all shallow slip with deep trench) values is  $0.934$ , with a standard deviation of  $0.222$ . Values  $>0.8$  are strongly indicative of presence of shallow slip with potentially enhanced tsunami amplitudes. This figure provides a summary of the potential for rapid determination of  $RMS_{P/C}$  from data at distances of  $30^\circ$  to  $80^\circ$ , giving 3–4 min faster contribution to tsunami excitation assessment than provided by the measurements in Figure 6.

It may be possible to enhance the performance for closer distance  $RMS_{P/C}$  measures by “masking out” the signals of  $PP$  and  $PPP$  or by using distance-varying time windowing for the  $P_{\text{coda}}$  duration, but we have kept this initial demonstration very simple, as is desirable for operational consideration. The  $P$  signal window can be quickly estimated from twice the centroid time for a rapid  $W$  phase moment tensor inversion, from time energy integrals of the broadband waveforms, or from simple inspection of the broadband data profiles, and a subsequent, comparable  $P_{\text{coda}}$  duration window defined with very straightforward data processing (instrument correction and band-pass filtering) with no other decisions, just time lagged for enough stations to provide good data averaging to constrain the event summary parameter.



**Figure 9.** Stacked spectra and spectral ratios of  $P$  (blue) and  $P_{\text{coda}}$  (red) ground velocity waveform segments of equal length band-pass filtered between 0.05 and 0.2 Hz for events with no shallow slip (top row) and events with shallow slip (bottom row). Individual station  $P_{\text{coda}}$  spectra were normalized to unity at 0.083 Hz, retaining correct relative amplitude of  $P$  spectra, and the median values at each spectral point for medians of  $10^\circ$  azimuthal bins for all  $P$  and  $P_{\text{coda}}$  measurements in the  $80^\circ$  to  $120^\circ$  distance range are plotted in each spectral comparison. Median values of the spectral ratios are shown below the spectra. The horizontal light magenta lines indicate the 7- to 15-s passband used for root-mean-square (RMS) calculations in  $RMS\_C/P$ . The short horizontal bold magenta lines indicate the 12- to 13-s spectral window used for narrowband spectral ratio comparisons shown in Figure 10. Figure S1 shows corresponding spectra for the  $30^\circ$  to  $80^\circ$  distance range. All corresponding event spectra are shown in Figure Bundles S1 and S2.

#### 4. Spectral Amplitude Measures for Interplate Thrust Events

The waveform profiles in Figure 4 suggest that frequency domain approaches should be promising for characterizing the  $P_{\text{coda}}/P$  behavior as an alternative to the time domain RMS amplitude measures discussed so far. Each seismogram could be converted to a spectrogram, seeking persistent narrowband features that correspond to prolonged  $pwP$  ringing. As a first approach to such frequency domain measures, intended to keep procedures simple, we compute the spectra for 5- to 20-s band-pass filtered ground velocity waveforms in the

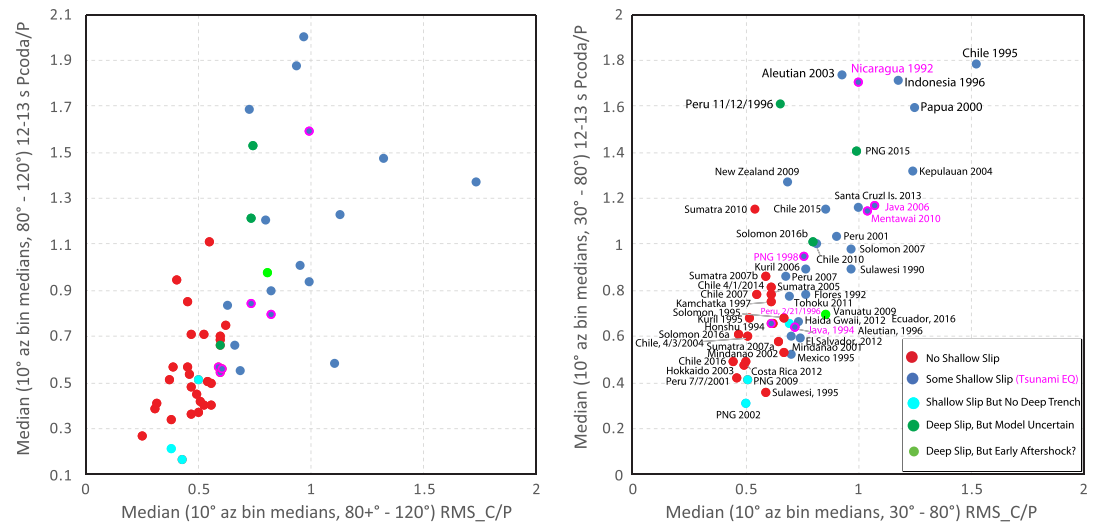


**Figure 10.** Comparison of narrowband spectral ratio measures of  $P_{\text{coda}}/P$  averaged over the 12- to 13-s range with  $\text{RMS}_C/P$  for interplate thrust events in the epicentral distance ranges  $80^{\circ}$  to  $120^{\circ}$  (left) and  $30^{\circ}$  to  $80^{\circ}$  (right). The median values of  $10^{\circ}$  azimuthal bin medians are shown for both measures. The data are color coded as in Figure 1.

$P$  and  $P_{\text{coda}}$  signal windows, stacking the observations to obtain event-specific spectra. We use the same  $P$  durations as in the RMS analysis, but we now make the  $P_{\text{coda}}$  durations exactly the same as the  $P$  durations for each event, to ensure uniform signal window lengths for spectral power estimates. The spectral amplitude at  $\sim 12$ -s period for each  $P_{\text{coda}}$  window is set to unity, with the relative scaling of the corresponding  $P$  window spectra being retained, and the spectra are stacked separately (using median values at each frequency for medians in  $10^{\circ}$  azimuthal bins) along with corresponding stacking of the  $P_{\text{coda}}/P$  spectral ratios for all stations in various distance ranges. Figure 9 shows examples of the median spectra for four events with no shallow slip (Figures 9a to 9d) and four events with shallow slip (Figures 9e to 9h). Corresponding spectra for the  $30^{\circ}$  to  $80^{\circ}$  distance window are shown in supporting information Figure S1, and all interplate thrust event spectra for the two distance windows are shown in supporting information Figure Bundles S1 and S2.

Thin magenta horizontal lines in the lower part of each spectral panel of Figure 9 indicate the band pass used for the RMS calculations (7 to 15 s or 0.067 to 0.143 Hz). The relative  $P$  and  $P_{\text{coda}}$  spectra in this passband control the measures in Figure 6. For the events with no shallow slip (top row), the  $P$  spectra (blue) are higher than the  $P_{\text{coda}}$  spectra (red) across the full bandwidth of the RMS measures, whereas for the events with some shallow slip (lower row), the  $P_{\text{coda}}$  spectra are higher than or similar to the  $P$  spectra over the lower-frequency part of the passband. The large peaks in  $P_{\text{coda}}$  spectra for the 1995 Chile and 2003 Aleutian events correspond to the high  $\text{RMS}_C/P$  values for these stations in Figure 6. Note that the stacked spectral ratios (Figures 9e' and 9f') have clear peaks around 0.07 Hz for these two events. The 2010 Mentawai earthquake has a spectral ratio peak near 0.10 Hz (Figure 9g'), consistent with the shallower depth of the trench in the source region. The spectra for the 2011 Tohoku event (Figure 9h) have relatively high spectral ratios (Figure 9h') over the whole bandwidth but no single large peak; this is likely due to the very broad extent of large slip from 30- to 7-km depth for this event (e.g., Yamazaki et al., 2018), which generated  $pwP$  with a broad spectrum of interfering resonances. As in Figure 6, the  $P_{\text{coda}}/P$  behavior clearly suggests the presence of shallow slip for 2011 Tohoku but not as dramatically as one might have expected given the 50+-m estimates of slip near the trench (e.g., Fujiwara et al., 2011; Sun et al., 2017). The lack of seaward observations with stable signals is possibly a factor in this, but the wide depth distribution of slip is likely the dominant factor.

Noting the large, narrowband peaks in the  $P_{\text{coda}}$  spectra for the 1995 Chile and 2003 Aleutian events in Figure 9, targeting the corresponding frequency band more selectively may hold promise of improving the recognition of deep water  $pwP$ . We take the average  $P_{\text{coda}}/P$  spectral ratio at periods from 12 to 13 s (0.077 to 0.083 Hz; the range of the short bold magenta lines in the lower portion of each spectral plot in

Figure 9), as a very specific search for deep water *pwP*. For the Tohoku event there is a small peak around 0.083 Hz in the spectral ratios as well, and much lower spectral ratios are observed for the events without shallow slip. Again, computing medians of medians in 10° azimuth bins for these 12- to 13-s period spectral ratios, we compare their behavior with the median *RMS\_C/P* measurements with similar binning for 80+° to 120° and 30° to 80° data sets in Figure 10. The event values are listed in Table S2. There is larger scatter than for comparison of RMS measurements as in Figure 7, but low or high spectral ratios and *RMS\_C/P* do separate the populations well. The correlation coefficient for the 80° to 120° measures is  $r = 0.684$ , while that for the 30° to 80° measures is  $r = 0.770$ . There is somewhat more population overlap in this narrowband spectral ratio, but this is likely an outcome of variable frequency deep water resonances due to trench depth variations among the different events, combined with the greater intrinsic variance of narrowband spectral measures. Consideration of full spectrograms that retain broader bandwidth may provide stabilization with respect to both of these aspects, but that is best suited to a neural network-based classification approach rather than the simple parametric approaches in this paper; that approach is being pursued separately.

## 5. Coda Magnitude and $m_B$ Measures for Interplate Thrust Events

Magnitude-based measures are also attractive for rapid applications in tsunami warning, largely due to the simplicity of the measurements and their widespread familiarity. While the *RMS\_C/P* measures are very straightforward, they do not provide absolute source strength levels due to lack of geometric spreading corrections or direct calibration with  $M_W$ . Tsunami warning approaches currently make use of the broadband body wave magnitude  $M_{WP}$  (e.g., Hirshorn et al., 2013) and *W* phase  $M_W$ , but there is also value in the classic body wave magnitude  $m_B$  when computed for *P* wave signals with periods around 3.5 s (e.g., Kanamori & Ross, 2019). As a relatively short period measure, comparison of  $m_B$  with  $M_W$  can robustly isolate tsunami earthquakes due to their deficient radiation of shorter period signals. We apply the same simple processing as used for  $m_B$  to our data and measure event median  $m_B$  values for each event. Then we use the same magnitude formulation to develop a corresponding coda magnitude,  $m_{coda}$ , for the period range of *pwP*, and consider a differential magnitude  $m_{coda} - m_B$ , as a proxy for *pwP* excitation, comparing it with *RMS\_C/P*.

The procedure used for  $m_B$  calculation exactly follows that of Kanamori and Ross (2019); broadband vertical component recordings are corrected to Weichert-type seismograph recordings; the instantaneous amplitude ( $A_P$ ) and period ( $T_P$ ) are measured and corrected to ground motion amplitude. The centroid time relationship  $t_c = 1.2 \times 10^{-8} M_0^{1/3}$  (Duputel et al., 2013; with  $M_0$  being the independently estimated seismic moment in dyne cm) is used to define a *P* wave duration window of  $3t_c$  (cutting it at the arrival time of *PP*, if necessary), and the magnitude is computed using  $m_B = \log_{10}(A_P/T_P) + Q(\Delta, h)$ , where  $Q(\Delta, h)$  is the Gutenberg and Richter distance ( $\Delta$ ), depth ( $h$ ) correction (Richter, 1958). The distance range for which the latter corrections are reliable does not extend to diffracted distances, so we limit magnitude measurements to the 30° to 80° range. Dominant periods of the measurements used in the  $m_B$  magnitudes are ~ 3 to 4 s.

The same magnitude formalism is used to estimate a  $P_{coda}$  magnitude,  $m_{coda}$ , but the broadband ground displacement data are filtered in the passband 8 to 15 s (typical  $T_P$  are in the range 11 to 14 s), and the  $P_{coda}$  time window is from  $5t_c$  to  $8t_c$  (or until the *S* arrival). We also consider durations of  $3t_c$  to  $6t_c$ , but for several events with long tails on their moment rate functions the later window better isolates the coda. As is the case for the *RMS\_C/P* measures, *PP* and *PPP* contaminate the  $m_{coda}$  measures at closer distances; hence, median values are used. The  $m_{coda}$  measures have the added attribute of being magnitudes that retain source strength information, but they are also single peak measures rather than RMS values so they are more sensitive to contamination from large late arrivals like *PP*, whereas RMS values intrinsically emphasize sustained large amplitudes throughout the coda window. The  $m_B$  and  $m_{coda}$  magnitudes and their differentials are listed in Table S2.

The differential median  $m_{coda} - \text{median } m_B$  measures (30° to 80°) are compared with the 80+° to 120° median *RMS\_C/P* values in Figure 11. As a result of measuring the ~12-s period coda strength versus the ~3.5-s period *P* strength in the magnitude differences, the differentials are particularly effective at separating the moderate size tsunami earthquakes from other events of similar size that rupture to shallow depth. The magnitude differences have more overlap of the bimodal population, and the correlation coefficient with the RMS measures is 0.598, but at the end of the range there is very good separation for shallow-slip (small magnitude difference) and deep-slip (large magnitude difference) events. The corresponding comparison using

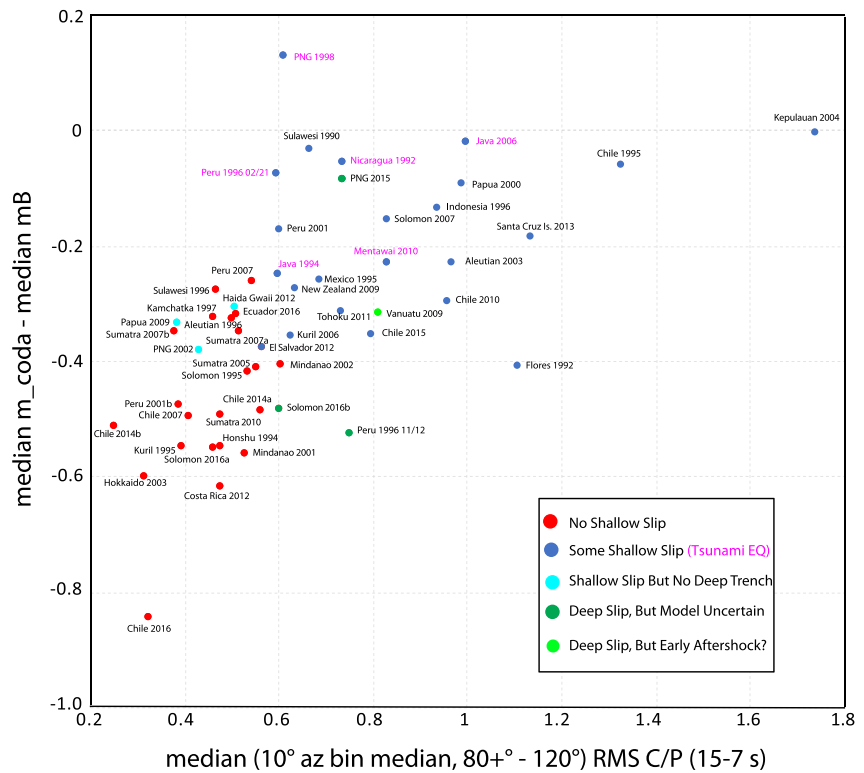


**Figure 11.** Comparison of median  $m_{coda} - m_B$  measures from the distance range  $30^\circ$  to  $80^\circ$  with median  $RMS_{C/P}$  for interplate thrust events in the epicentral distance range  $80^\circ$  to  $120^\circ$  using medians of  $10^\circ$  azimuthal bins. The data are color coded as in Figure 1.

the  $30^\circ$  to  $80^\circ$  median  $RMS_{C/P}$  values is shown in Figure 12, with similar general behavior and an overall correlation coefficient of 0.730. Using the  $3t_c$  to  $6t_c$  window for the coda duration for  $m_{coda}$  (see Figures S2 and S3) gives measures with  $\sim 0.16$  lower correlation coefficients for the two distance ranges.

Given that all of the RMS and spectral and magnitude differential measures can be processed very rapidly, various measures may be combined in artificial intelligence frameworks to optimize population classification. Again, this is left for future efforts; the bimodal classification of updip extent of rupture that we have adopted is very simplified and may not represent the continuum of actual earthquake behaviors that contribute to fuzziness and overlap of the parametric measures that we explore here. That aspect of the problem must be considered further in more complex classification schemes. Practically speaking, very sophisticated approaches (such as finite-fault modeling or other procedures requiring many user decisions) are of limited use for rapid tsunami warning decision making. The simple parametric behaviors observed here give the primary contribution of coda-based approaches; observation of high relative  $P_{coda}$  levels (large  $RMS_{C/P}$ , small  $m_{coda} - m_B$ , large 12- to 13-s  $P_{coda}/P$  spectral ratios) suggests shallow slip which is expected to enhance tsunami excitation, and in combination with a  $W$  phase determination of mechanism geometry and seismic moment, the added information about rupture depth can add confidence in the warning and provides emphasis that a larger than typical tsunami might have been generated.

### 6. Coda Measurements for Other Types of Large Shallow Events

Thus far, our focus has been on known interplate thrust-faulting ruptures in subduction zones. There are other types of large earthquakes of concern for tsunami generation, including interplate thrust-faulting events, normal-faulting events, and some near-coastal strike-slip events. Figure 5 shows the global distribution of large earthquakes from 1990 to 2018, highlighting the nonmegathrust events in red. For all 34 of the latter events, we computed  $RMS_{C/P}$ ,  $m_{coda} - m_B$ , and 12- to 13-s period  $P_{coda}/P$  spectral amplitude ratios (Tables S1 and S2), using the same procedures applied to the megathrust events. Comparison of  $m_{coda} -$

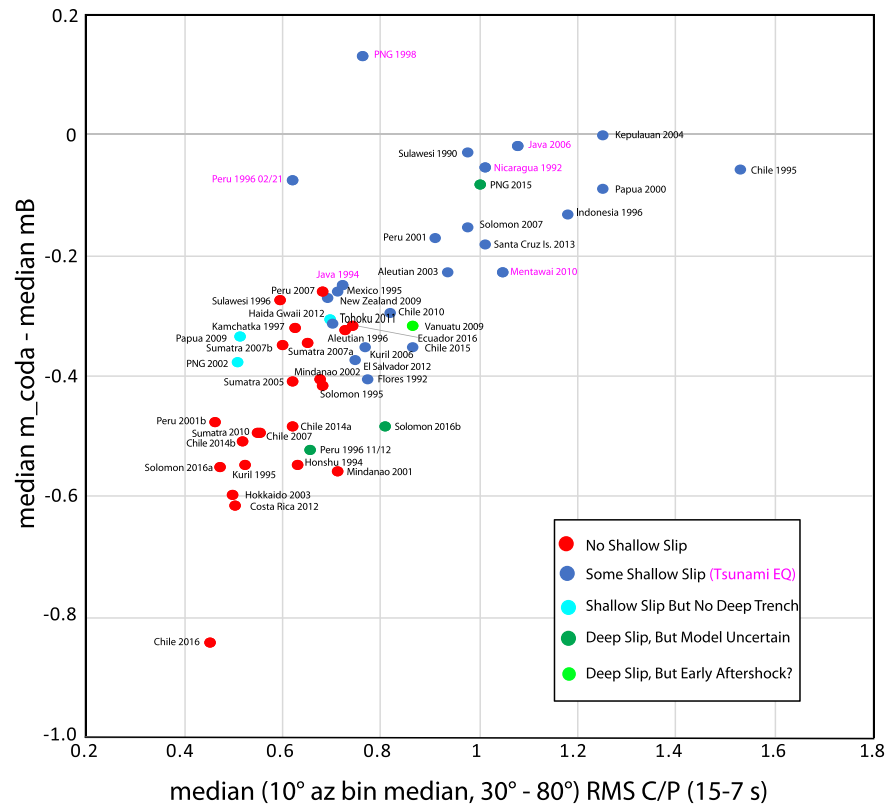


**Figure 12.** Comparison of median  $m_{coda} - m_B$  measures from the distance range  $30^\circ$  to  $80^\circ$  with median  $RMS_{C/P}$  for interplate thrust events in the epicentral distance range  $30^\circ$  to  $80^\circ$  using medians of  $10^\circ$  azimuthal bins. The data are color coded as in Figure 1.

$m_B$  and  $80-120^\circ RMS_{C/P}$  measures in Figure 13 establishes that there is a large range in relative coda levels, comparable to that for interplate thrust events, and there is good correlation ( $r = 0.734$ ) between these parametric measures. The events are color coded according to mechanism type.

Strike-slip events systematically tend to have larger relative coda levels, particularly for the RMS measures, which is probably a manifestation of both close to nodal downgoing  $P$  radiation and strong near-source scattering due to the  $P$  and  $SH$  radiation patterns having radiation lobes in the horizontal directions. Note that the strike-slip events with the largest relative coda levels are interplate ruptures on transform faults, which rupture primarily within the crust. Intraplate strike-slip events have lower coda, notably for the large events in the Wharton basin, which have relatively large centroid depths (Lay, 2019). The two continental strike-slip events (2001 Kunlun and 2002 Denali) have moderate to low coda levels that must be generated by scattering rather than  $pwP$ . The same is true for the six continental thrust events, and it is notable that the coda levels for these events span a range similar to that for suboceanic thrusts in backarcs, outer rise oceanic lithosphere, and subducted slabs. The latter three populations have measures comparable to those for interplate thrusts that lack shallow slip. The back-arc thrust events are similar to the outliers in Figures 6 and 8 for thrust events with shallow slip but no deep trench in which to generate long-period  $pwP$ . The 1999 Vanuatu event did generate local 7-m tsunami runup (Regnier et al., 2003), so these events can be tsunamigenic, but their locations immediately identify them as distinct from megathrust events. The intraplate thrusts in the outer rise and in slabs tend to have greater depths than the megathrust ruptures, accounting for their weak excitation of  $pwP$  contributions to  $P_{coda}$ . Tsunamigenic normal-faulting events in the outer rise (e.g., 2007 Kuril and 2009 Samoa) have higher coda levels than deeper intraslab normal fault ruptures such as the 2001 El Salvador and 2017 Chiapas.

Given that some of these events are tsunamigenic, we compare the  $RMS_{C/P}$  measures obtained for different distance intervals ( $30^\circ$  to  $120^\circ$  and  $30^\circ$  to  $80^\circ$ ) with the results for  $80^\circ$  to  $120^\circ$  (free of any  $PP$  contamination) in Figure 14. The correlations are high ( $r = 0.932$  to  $0.978$ ), indicating that measures made at closer distances

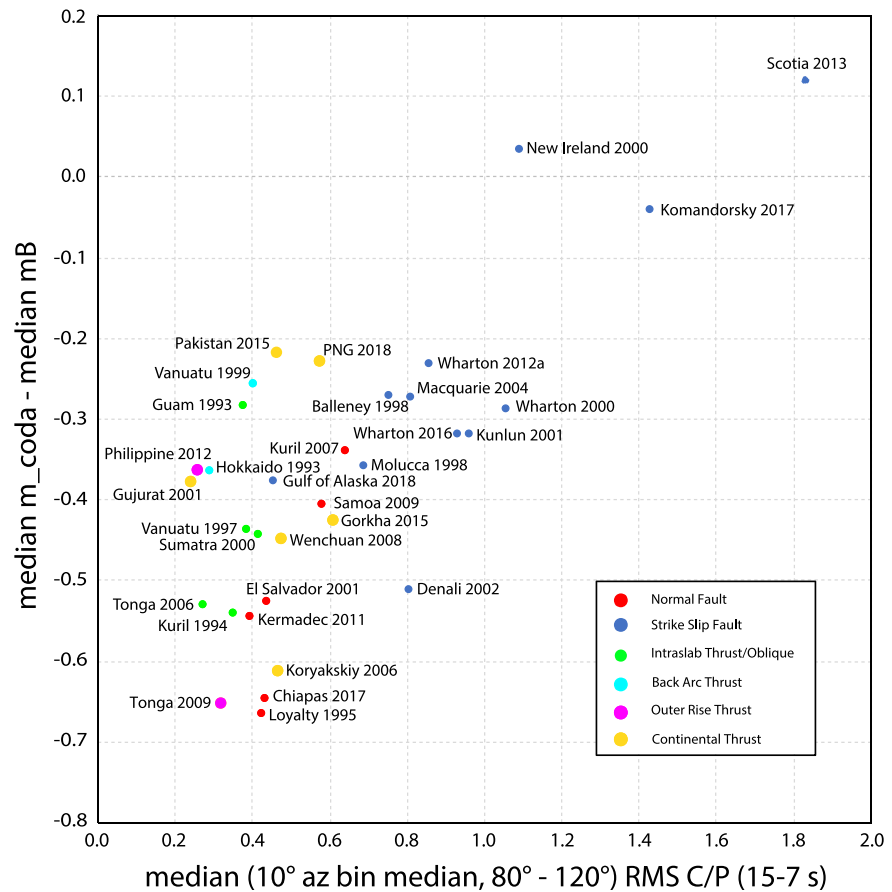


**Figure 13.** Comparison of median  $m_{coda} - m_B$  measures from the distance range  $30^\circ$  to  $80^\circ$  with median  $RMS_{C/P}$  for intraplate and strike-slip transform faulting in the epicentral distance ranges  $80^\circ$  to  $120^\circ$  using medians of  $10^\circ$  azimuthal bins. The data are color coded by mechanism type and tectonic setting.

can help in tsunami warning assessment for these nonmegathrust events, informed by the moment tensor faulting geometry. Given an offshore faulting mechanism with significant dip-slip component, the  $P_{coda}$  excitation levels can again contribute to assessment of likelihood that shallow faulting under deep water has enhanced tsunami excitation or not. Using  $P_{coda}$  to recognize the shallow rupture of the thrust events under shallow water will require calibration of signals in the frequency band 5–7 s. For strike-slip events, the indication of shallow depth rupture for the transform faulting environments versus the intraplate environments also provides useful information, although tsunami excitation will intrinsically likely be modest with possible exception of events that rupture from offshore to onshore.

### 7. Discussion of How $P_{coda}$ Measures Can Help Improve Tsunami Warning

Simple parametric measures of seismic wavefields from large offshore earthquakes can be obtained in near real time due to open access to and telemetry of global broadband stations. This data availability underlies the ability to quickly determine broadband magnitudes, to invert long-period ground motions for the moment tensor, to evaluate radiated energy, and even to formulate rapid finite-fault inversions. However, resolving the updip extent of slip in thrust faulting events, particularly on megathrusts, remains challenging for rapid analyses. Onshore geodetic data have expanding global deployment and rapid processing but also intrinsically do not resolve the far offshore slip distribution for megathrust failures. Real-time data from offshore geodetic sites can resolve this problem but remain very limited in coverage globally. When rupture extends to near the trench, there is enhanced generation of tsunami signals for an event of a given size (Figure 2). This is the essence of shallow-rupturing tsunami earthquakes (Kanamori, 1972), which may be

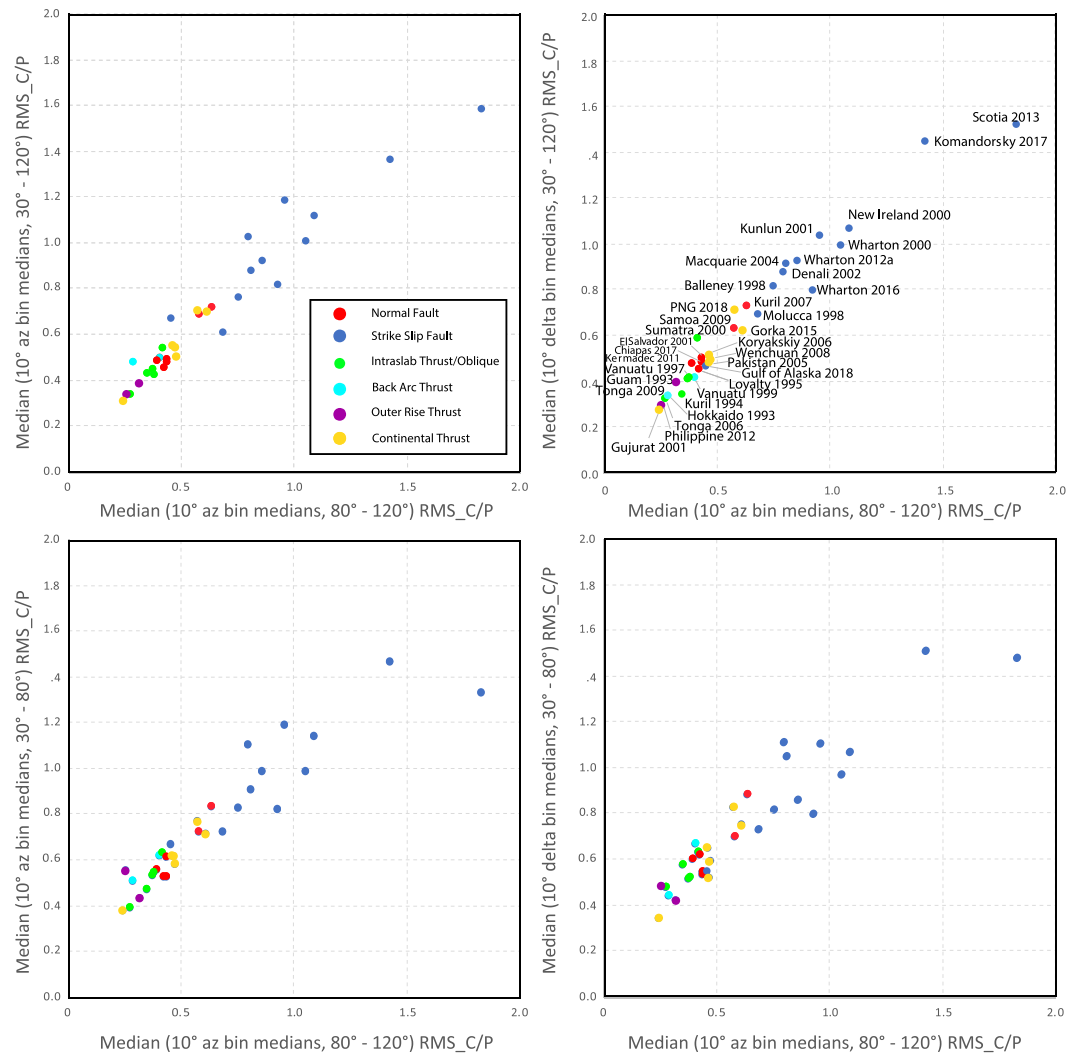


**Figure 14.** Comparison of  $RMS\_C/P$  measures for intraplate and strike-slip transform events made using different distance ranges and data binning. The top row compares median  $RMS\_C/P$  for data spanning the distance range  $30^\circ$  to  $120^\circ$  using medians of  $10^\circ$  azimuthal bins (left) or  $10^\circ$  distance bins (right) with median  $RMS\_C/P$  for data spanning the range  $80^\circ$  to  $120^\circ$  with  $10^\circ$  azimuthal bins. The lower row compares median  $RMS\_C/P$  for data spanning the distance range  $30^\circ$  to  $80^\circ$  using medians of  $10^\circ$  azimuthal bins (left) or  $10^\circ$  distance bins (right) with median  $RMS\_C/P$  for data spanning the range  $80^\circ$  to  $120^\circ$  with  $10^\circ$  azimuthal bins. Color coding corresponds to Figure 13, indicating the faulting type. Note that the various thrust fault types all have low coda levels.

quickly recognizable based on their deficient short-period amplitude spectrum, but it also holds for ruptures spanning a wide portion of the megathrust such as the 2011 Tohoku and 2010 Chile earthquakes (e.g., Maksymowicz et al., 2017; Yue et al., 2014), which do not register as tsunami earthquakes. As shown here, assessment of long-period  $pwp$  seismic wave arrivals, which are expected to be preferentially generated by shallow slip under deep water, can help to resolve this issue.

When a large earthquake occurs, if regional seismic and seismogeodetic ground motions are available for rapid processing, the faulting mechanism and seismic moment or average fault slip and the along-strike faulting dimensions can be determined within  $\sim 3$  to 15 min after the hypocentral time, depending on event location and station distribution. To supplement that information, the various parametric  $P_{\text{coda}}/P$  measures described here can add the important nuance of whether the faulting extended into deep water (near the subduction zone trench), and if so, that tsunami excitation may be stronger than typical for the event's magnitude by up to the factor of 2 to 3 increase observed for tsunami earthquakes relative to comparable

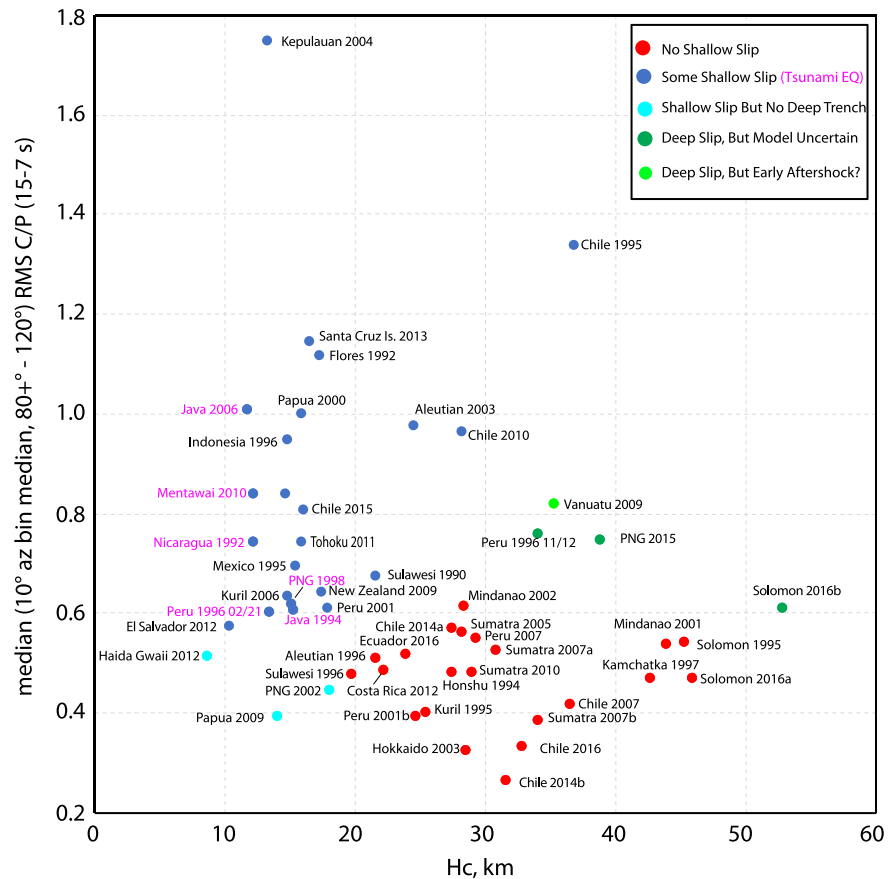


**Figure 15.** Median  $RMS\_C/P$  for medians of  $10^\circ$  azimuthal bins for the  $80+^\circ$  to  $120^\circ$  megathrust data set plotted versus  $H_c$ , the centroid depth of slip distribution listed in Table 1 for the 52 interplate thrust events considered in this study. The data are color coded as in Figure 1.

seismic moment events deeper on the megathrust (Figure 2). The  $RMS\_C/P$  and other coda measures alone do not provide direct prediction of tsunami amplitudes; that can be inferred best in combination with the  $W$  phase moment tensor and/or geodetic observations. What is added by these measures is information about the updip extent of rupture, which is hard to rapidly constrain otherwise (and intrinsically, improved constraint on the overall rupture depth, which can be quite uncertain in rapid  $W$  phase inversions using sparse data). Figure 15 compares the median  $RMS\_C/P$  measures for interplate thrusts using the  $80+^\circ$  to  $120^\circ$  data set with the  $H_c$  values from finite-fault models (Table 1). Large coda levels are strong indicators of shallow slip under deep water, which is connected to shallow  $H_c$ . Low  $RMS\_C/P$  is strongly indicative of deeper  $H_c$ . The coda information can be obtained within  $\sim 15$  min after the event starts, and as more distant data become available, increasing confidence can be attached to the resulting measures and inferences. This is much sooner than the determination of reliable slip models from finite-fault inversions needed for direct estimation of  $H_c$ .

Figure 16 directly compares median  $RMS\_C/P$  measures with  $\log_{10}$  (maximum water height;  $\log MWH$ ). There is a general tendency for larger coda to be associated with larger tsunami amplitude, but it is important to note that absolute event size information is not represented by the coda ratio (the highly scattered variation of these  $RMS\_C/P$  measures with  $M_W$  is shown in Figure S4). In order to account for the contribution of event size, we consider the two populations in the interplate thrust event data set in Figure 1. Figure 17 shows separate regressions of  $\log MWH$  on  $M_W$  for the event subpopulations with at least some shallow slip (blue points) or no shallow slip (red points), omitting the ambiguous events with no tsunami reported, uncertain faulting models, or shallow slip but no deep water trench. The two populations have some scatter and overlap, but the influence of shallow rupture is strongly indicated, with convergence of the curves for very

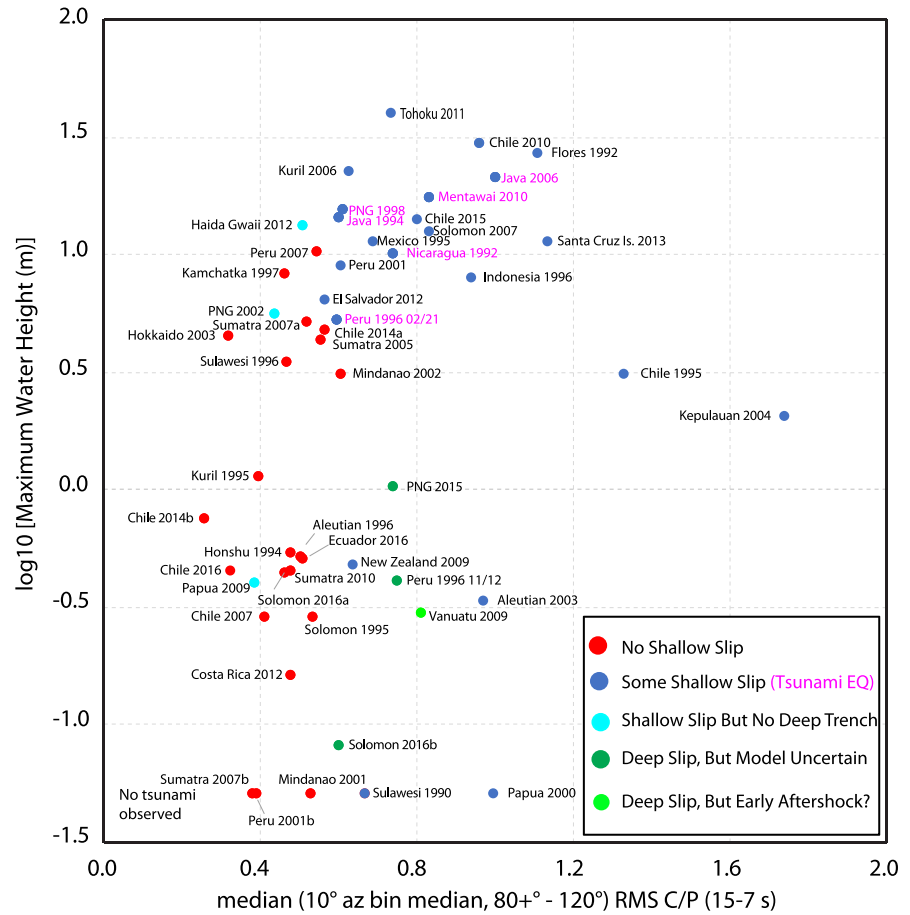


**Figure 16.**  $\log_{10}$  of the maximum water height reported by the National Oceanic and Atmospheric Administration versus median  $RMS\_C/P$  for medians of  $10^\circ$  azimuthal bins of the  $80^\circ$  to  $120^\circ$  data set for the 52 interplate thrust events considered in this study. No tsunami was reported for the five events located at the bottom. The data are color coded as in Figure 1.

large ruptures near magnitude 9. The regression for the events with no shallow slip has a slope close to 1, indicating that for deeper rupture, maximum water height roughly scales directly with  $M_W$  for this subpopulation.

We use the behavior in Figure 17 to adjust the maximum water height measures for effects of varying  $M_W$ , allowing us to compare directly with the coda measurements. To remove the magnitude effect, we assume the form shown in Figure 17 for the events lacking shallow slip:

$$\log MWH = aM_w + b \quad (1)$$

Since  $MWH$  given in Table 1 is only a first-order characterization of the tsunami, here we use a slope  $a = 1.0$  for simplicity, with corresponding  $b = -7.9$ . Since Abe's (1979) tsunami magnitude,  $M_t$ , defined as a linear relationship,  $M_t = \log H + B$  ( $H$  is the tsunami amplitude), is generally compatible with  $M_W$ , the choice of  $a = 1$  is reasonable. Then,  $\Delta(\log MWH) \equiv \log MWH - (aM_w + b)$  can be interpreted as the enhanced water height caused by shallow slip.

Figures 18–20 show how  $\Delta(\log MWH)$  depends on the various measures of shallow slip. Figure 18 plots the resulting magnitude-corrected maximum water height values versus  $H_c$ , demonstrating the clear influence of slip depth on enhancement of the water height. This figure can be compared to Figure 2 to see that the trend is slightly enhanced by the magnitude correction. The correlation coefficient for only the red and blue populations in Figure 2 is  $-0.529$ , whereas for the same subgroup in Figure 18 it is  $-0.575$ . Figure 19

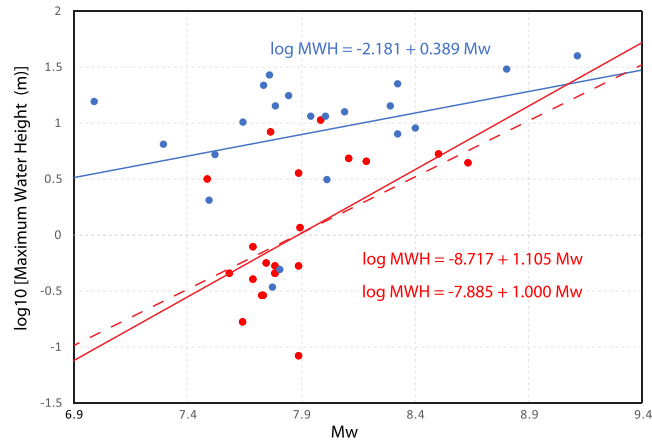


**Figure 17.** Examination of trends in the data from Figure 1 for the subpopulations of events with shallow slip (blue circles) and events with no shallow slip (red circles) for  $\log_{10}$  of the maximum water height (MWH) versus  $M_W$ . Note the quasi-linear relationship between  $\log_{10}(\text{MWH})$  and  $M_W$  for the events with no shallow slip. Regressions with unconstrained slope and slope of 1 are shown.

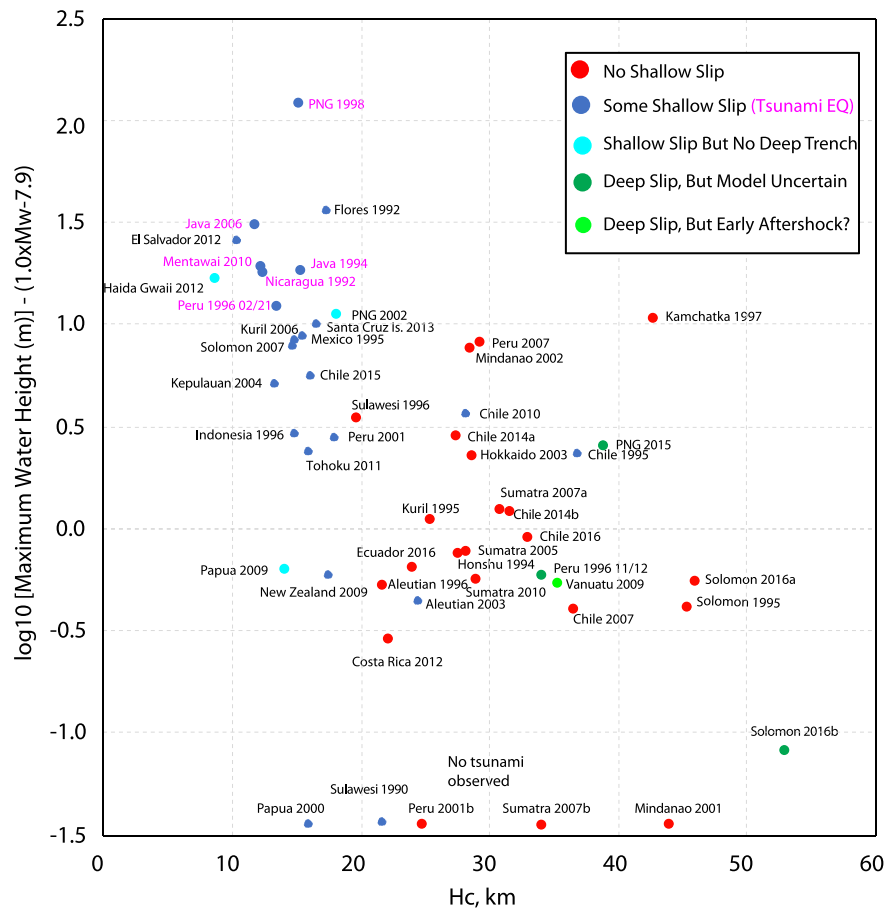


**Figure 18.**  $\log_{10}$  of the maximum water height reported by the National Oceanic and Atmospheric Administration, scaled for event size by subtracting  $(1.0 \times M_W - 7.9)$ , versus  $H_c$ , the centroid of the slip distribution for the finite-faults reported in Table 1 for the 52 interplate thrust events considered in this study. No tsunami was reported for the five events located at the bottom. The data are color coded as in Figure 1.

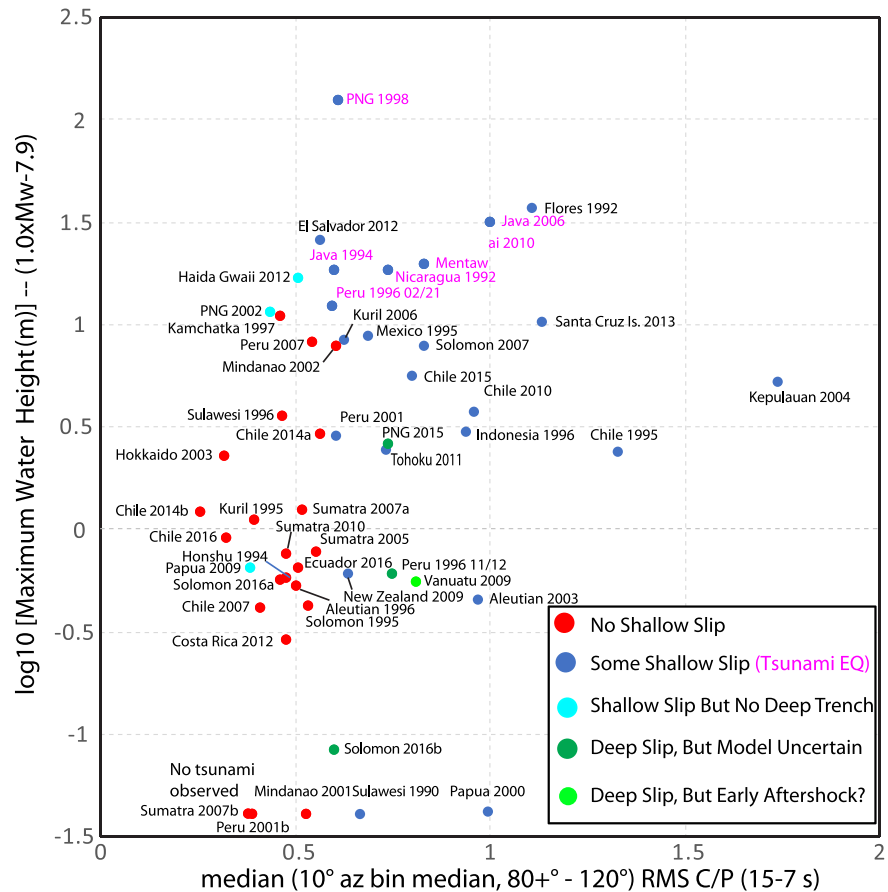


**Figure 19.**  $\log_{10}$  of the maximum water height reported by the National Oceanic and Atmospheric Administration, scaled for event size by subtracting  $(1.0 \times M_W - 7.9)$ , versus median  $RMS\_C/P$  for medians of  $10^\circ$  azimuthal bins of the  $80^\circ$  to  $120^\circ$  data set for the 52 interplate thrust events considered in this study. No tsunami was reported for the five events located at the bottom. The data are color coded as in Figure 1.

makes a similar comparison of magnitude-corrected maximum water height values versus median  $RMS\_C/P$  for the  $80^\circ$  to  $120^\circ$  data with  $10^\circ$  azimuthal bin medians. This can be compared with Figure 16, with the effects of  $M_W$  scaling of the maximum tsunami height now being suppressed. The scatter is substantial, and the correlation does not change significantly (for the red and blue points it is 0.361 in Figure 16 and 0.346 in Figure 18). It is quite possible that large  $pwP$  can be generated by modest slip at shallow depth, so there need not be strong tsunami excitation for a large  $RMS\_C/P$ . The 2003 Aleutian event is an example; it has a high coda level but only small reported tsunami. For this event slip does occur at shallow depth but it is only  $\sim 1$  m (Ye et al., 2016). The strong coda produced indicates high efficiency of generation of  $pwP$  by relatively minor slip. Alternatively, tsunami can be enhanced by submarine slumping; this appears to hold for the 1998 Papua tsunami earthquake (e.g., Synolakis et al., 2002; Tappin et al., 2008). Figure 20 compares the magnitude-corrected maximum water height values with  $m_{coda} - m_B$  measurements. This comparison has a relatively high correlation of 0.591 for the subset of red and blue points, improved from a 0.302 correlation with the uncorrected values. The enhanced separation of the tsunami earthquakes by the differential magnitude measurement is responsible for the stronger correlation.

We can perform linear regressions on how  $\Delta(\log MWH)$  depends on the various parameters,  $p$ :

$$\Delta(\log MWH) = cp + d \quad (2)$$

to determine the coefficients  $c$  and  $d$ . The linear representation is entirely empirical, not physics based. Once  $c$  and  $d$  are determined, we can estimate the enhanced water height using (2) for a measured  $p$ . Alternatively,

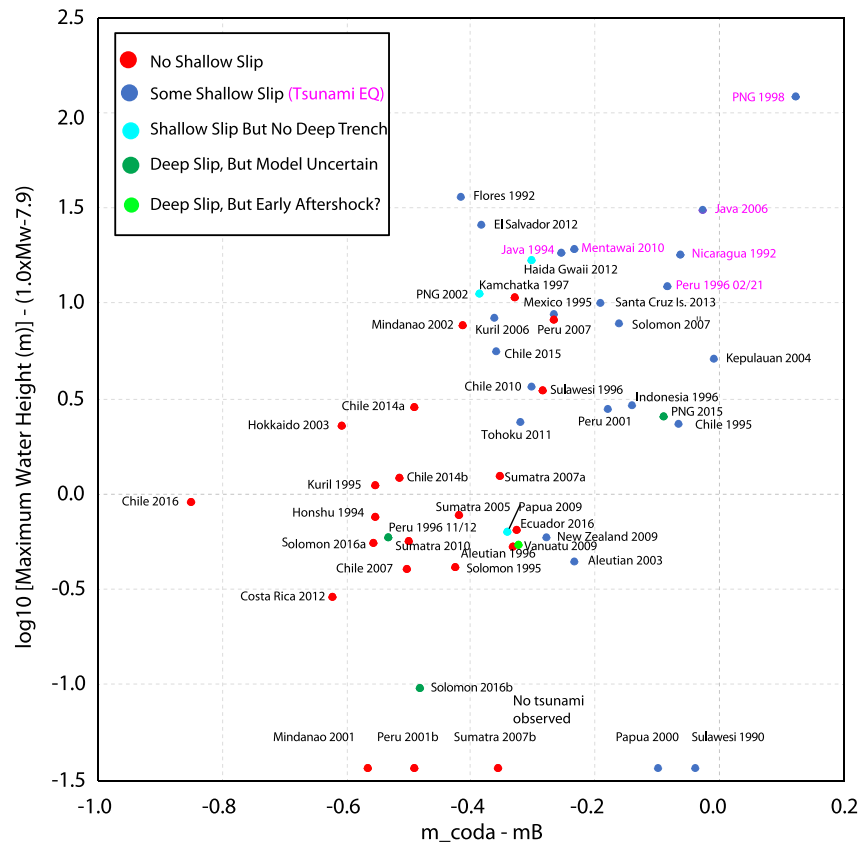


**Figure 20.**  $\log_{10}$  of the maximum water height reported by the National Oceanic and Atmospheric Administration, scaled for event size by subtracting  $(1.0 \times M_W - 7.9)$ , versus median  $m_{\text{coda}} - m_B$  for the 52 interplate thrust events considered in this study. No tsunami was reported for the five events located at the bottom. The data are color coded as in Figure 1.

since the slope of equation (1) is 1,  $\Delta(\log MWH)$  can be also interpreted as an effective increment of magnitude,  $\Delta M_w = cp + d$ , if we are to estimate the enhanced water height in terms of an increased  $M_w$ .

For example, the linear regression of  $\Delta \log MWH$  on median  $RMS\_C/P$  ( $80^\circ +/120^\circ$ ) has slope  $c = 0.7702$  and intercept  $d = -0.0273$ , and the same regression on  $m_{\text{coda}} - m_B$  has  $c = 1.99$  and  $d = 1.14$ . These regressions omit events with no tsunami detection, uncertain slip models, shallow slip under shallow water, or early aftershock contamination. Using these values of  $c$  and  $d$ , we get  $\Delta M_w = 0.54$ ,  $0.54$ , and  $0.22$  (for  $p = RMS\_C/P$ ) and  $0.51$ ,  $1.02$ , and  $-0.06$  (for  $p = m_{\text{coda}} - m_B$ ) for the 2011 Tohoku ( $M_w = 9.1$ ), 1992 Nicaragua ( $M_w = 7.7$ ), and the 2003 Hokkaido ( $M_w = 8.2$ ) events, respectively. This illustrates how the occurrence of coda-generating shallow slip can be mapped into an effective magnitude increase that controls maximum water height. We tabulate  $\Delta M_w$  for all of the earthquakes used in the regressions in Table S3.

This regression-based approach can be formalized with propagation of errors, but the ambiguous nature of the maximum water level values and the scatter in the correlations with coda parameters may not warrant very precise calculations. As a conservative approach, tsunami warnings based primarily on rapid faulting mechanism, seismic moment, and coastal deformation observations can be given added emphasis on the tsunami likely being higher than normal if the coda measures are indicative of at least some slip on the shallow megathrust having occurred.

It is also important to recognize that large coda can be observed for some events with only modest shallow slip (and low tsunami excitation). The 2013 Aleutian and 1995 Chile events are clear examples of this. The generation of  $pwp$  is, of course, more complex than simple vertical reverberations above the source, and in detail it depends on 3-D geometry of the bathymetry and the presence of low-velocity sediment structures. Detailed 3-D modeling of subduction environments (e.g., Qian et al., 2019; Wu et al., 2018) may help to

identify improved metrics sensitive to occurrence of shallow slip and  $pwP$  excitation along with recognition of structural scattering that can generate  $pwP$  laterally offset from the slip zone (e.g., Fan & Shearer, 2018; Yue et al., 2017).

## 8. Conclusions

Use of  $\sim 12$ -s  $P_{\text{coda}}$  amplitude relative to  $P$  as a measure of  $pwP$  generation by slip at shallow depth under deep water during megathrust ruptures has potential to enhance tsunami warnings, given that such slip can be particularly tsunamigenic. The initial work of Lay and Rhode (2019), using observations at large distances ( $>80^\circ$ ) for which there is almost always a seismogram interval free of expected arrivals between the end of the direct  $P$  wave signals from the rupture and the ensuing  $PP$  and  $PKIKP$  phases, established that higher  $P_{\text{coda}}$  levels relative to  $P$  correlate well with independent determinations of slip having occurred at shallow depths under deep water. This idea is extended here to closer distance data ( $30^\circ$  to  $80^\circ$ ) to reduce the lag time necessary to evaluate the relative level of  $P_{\text{coda}}/P$  to less than 15 min, making it more useful for tsunami warning decision making. Simple parametric measures, such as 7- to 15-s period RMS  $P_{\text{coda}}/\text{RMS } P$  ( $\text{RMS}_P/C$ ),  $m_{\text{coda}} - m_B$ , and 12- to 13-s  $P_{\text{coda}}/P$  spectral ratios, provide strong indication of the presence of some shallow slip under deep water (high values) or lack of slip under deep water (low values), so that nuance can be added to tsunami warnings based on seismic moment and faulting geometry (shallow slip under deep water suggesting potential for stronger than typical tsunami for a given event size). Calibration of the coda measurements for shorter periods may allow shallow slip under shallower maximum water depths to be recognized. It would be straightforward to precalculate the optimal  $pwP$  passband to consider for regions with different trench depths. Information about the slip distribution on the megathrust gleaned from  $P_{\text{coda}}$  levels has many other applications: for parameterization of finite-fault models, for evaluation of potential for ensuing tsunami earthquakes updip of megathrust failures that do not reach to the trench, and for assessment of frictional properties as a function of depth on subduction zone megathrusts.

## Acknowledgments

All of the broadband seismic waveforms used in this study were accessed from the Data Management Center of the Incorporated Research Institutions for Seismology (<https://www.iris.edu/hq/>). Centroid moment tensor solutions were obtained from the website (<https://www.globalcmt.org/>). Maximum water height values are primarily from the National Oceanic and Atmospheric Administration, available online ([https://www.ngdc.noaa.gov/hazard/tsu\\_db.shtml](https://www.ngdc.noaa.gov/hazard/tsu_db.shtml)). Lingling Ye provided helpful waveform plotting software. We thank Associate Editor Diego Melgar, reviewer Andrew Newman, and an anonymous reviewer for their comments on the manuscript. T. Lay's research on earthquakes is supported by the U.S. National Science Foundation Grant EAR1802364. C. Liu was supported by the National Key R & D Program on Monitoring, Early Warning and Prevention of Major Natural Disaster (2017YFC1500305) and the Visiting Scholar Program of the Chinese Science Council.

## References

- Abe, K. (1979). Size of great earthquakes of 1837-1974 inferred from tsunami data. *Journal of Geophysical Research*, 84(B4), 1561-1568. <https://doi.org/10.1029/JB084iB04p01561>
- Bernard, E., & Titov, V. (2015). Evolution of tsunami warning systems and products. *Philosophical Transactions Royal Society of London, A*, 373(2053), 20140371. <https://doi.org/10.1098/rsta.2014.0371>
- Blewitt, G., Kreemer, C., Hammond, W. C., Plag, H.-P., Stein, S., & Okal, E. (2006). Rapid determination of earthquake magnitude using GPS for tsunami warning systems. *Geophysical Research Letters*, 33, L11309. <https://doi.org/10.1029/2006GL026145>
- Colombelli, S., Allen, R. M., & Zollo, A. (2013). Application of real-time GPS to earthquake early warning in subduction and strike-slip environments. *Journal of Geophysical Research: Solid Earth*, 118, 3448-3461. <https://doi.org/10.1002/jgrb.50242>
- Duputel, Z., Rivera, L., Kanamori, H., Hayes, G. P., Hirshorn, B., & Weinstein, S. (2011). Real-time  $W$  phase inversion during the 2011 off the Pacific coast of Tohoku earthquake. *Earth, Planets and Space*, 63(7), 535-539. <https://doi.org/10.5047/eps.2011.05.032>
- Duputel, Z., Tsai, V. C., Rivera, L., & Kanamori, H. (2013). Using centroid time-delays to characterize source durations and identify earthquakes with unique characteristics. *Earth and Planetary Science Letters*, 374, 92-100. <https://doi.org/10.1016/j.epsl.2013.05.024>
- Fan, W., & Shearer, P. M. (2018). Coherent seismic arrivals in the  $P$  wave coda of the 2012  $M_W$  7.2 Sumatra earthquake: Water reverberations or an early aftershock? *Journal of Geophysical Research: Solid Earth*, 123, 3147-3159. <https://doi.org/10.1002/2018JB015573>
- Fujiwara, T., Kodaira, S., No, T., Kaiho, Y., Takahashi, N., & Kaneda, Y. (2011). The 2011 Tohoku-oki earthquake: Displacement reaching the trench axis. *Science*, 334(6060), 1240. <https://doi.org/10.1126/science.1211554>
- Guilhem, A., Dreger, D. S., Tsuruoka, H., & Kawakatsu, H. (2013). Moment tensors for rapid characterization of megathrust earthquakes: The example of the 2011  $M$  9 Tohoku-oki, Japan earthquake. *Geophysical Journal International*, 192, 759-772. <https://doi.org/10.1093/gji/ggs045>
- Hannemann, K., Lange, D., Kopp, H., Petersen, F., & Contreras-Rees, E. (2016). Monitoring deformation offshore northern Chile using a seafloor geodetic network (GeoSEA). *American Geophysical Union, Fall Meeting 2016*, abstract #T31C-2900.
- Hayes, G. P. (2017). The finite, kinematic rupture properties of great-sized earthquakes since 1990. *Earth and Planetary Science Letters*, 468, 94-100. <https://doi.org/10.1016/j.epsl.2017.04.003>
- Hirshorn, B., Weinstein, S., & Tsuboi, S. (2013). On the application of  $M_{wp}$  in the near field and the March 11, 2011 Tohoku earthquake. *Pure and Applied Geophysics*, 170(6-8), 975-991. <https://doi.org/10.1007/s00024-012-0495-3>
- Hoechner, A., Ge, M., Babeyko, A. Y., & Sobolev, S. V. (2013). Instant tsunami early warning based on real-time GPS—Tohoku 2011 case study. *Natural Hazards and Earth System Sciences*, 13(5), 1285-1292. <https://doi.org/10.5194/nhess-13-1285-2013>
- Ihmlé, P. F., & Madariaga, R. (1996). Monochromatic body waves excited by great subduction zone earthquakes. *Geophysical Research Letters*, 23(21), 2999-3002. <https://doi.org/10.1029/96GL02892>
- Kanamori, H. (1972). Mechanism of tsunami earthquakes. *Physics of the Earth and Planetary Interiors*, 4, 289-300.
- Kanamori, H., & Rivera, L. (2008). Source inversion of  $W$  phase: Speeding up seismic tsunami warning. *Geophysical Journal International*, 175(1), 222-238. <https://doi.org/10.1111/j.1365-246X.2008.03887.x>
- Kanamori, H., & Ross, Z. E. (2019). Reviving  $m_B$ . *Geophysical Journal International*, 216(3), 1798-1816. <https://doi.org/10.1093/gji/ggy510>
- Kanazawa, T., Uehira, K., Mochizuki, M., Shiingo, T., Fujimoto, H., Noguchi, S., et al. (2016). S-Net project, cabled observation network for earthquakes and tsunamis. *SubOptic*, 2016 (5 pp.).

- Lay, T. (2018). A review of the rupture characteristics of the 2011 Tohoku-oki  $M_W$  9.1 earthquake. *Tectonophysics*, 733, 4–36. <https://doi.org/10.1016/j.tecto.2017.09.022>
- Lay, T. (2019). Reactivation of oceanic fracture zones in intraplate earthquakes? In J. C. Duarte (Ed.), *Transform Plate Boundaries and Fracture Zones* pp. 89–104. Amsterdam: Elsevier. <https://doi.org/10.1016/B978-0-12-812064-4.00004-9>
- Lay, T., & Rhode, A. (2019). Evaluating the updip extent of large megathrust ruptures using  $P_{\text{coda}}$  levels. *Geophysical Research Letters*, 46, 5198–5206. <https://doi.org/10.1029/2019GL082774>
- Lay, T., Ye, L., Ammon, C. J., & Kanamori, H. (2017). Intraslab rupture triggering megathrust rupture coseismically in the 17 December 2016 Solomon Islands  $M_W$  7.9 earthquake. *Geophysical Research Letters*, 44, 1286–1292. <https://doi.org/10.1002/2017GL072539>
- Lay, T., Ye, L., Kanamori, H., Yamazaki, Y., Cheung, K. F., & Ammon, C. J. (2013). The February 6, 2013  $M_W$  8.0 Santa Cruz Islands earthquake and tsunami. *Tectonophysics*, 608, 1109–1121. <https://doi.org/10.1016/j.tecto.2013.07.001>
- Lee, S.-J., Lin, T.-C., Feng, K.-F., & Liu, T.-Y. (2018). Composite megathrust rupture from deep interplate to trench of the 2016 Solomon Islands earthquake. *Geophysical Research Letters*, 45, 674–681. <https://doi.org/10.1002/2017GL076347>
- Lorito, S., Romano, F., & Lay, T. (2016). Tsunamiogenic major and great earthquakes (2004–2013): Source processes inverted from seismic, geodetic, and sea-level data. In R. A. Meyers (Ed.), *Encyclopedia of Complexity and System Science* (pp. 1–52). New York: Springer Science + Business Media. [https://doi.org/10.1007/978-3-642-27737-5\\_641-1](https://doi.org/10.1007/978-3-642-27737-5_641-1)
- Maksymowicz, A., Chadwell, C. D., Ruiz, J., Tréhu, A. M., Contreras-Reyes, E., Weinreber, W., et al. (2017). Coseismic seafloor deformation in the trench region during the  $M_W$  8.8 Maule megathrust earthquake. *Scientific Reports*, 7(1). <https://doi.org/10.1038/srep45918>
- Melgar, D., Allen, R. M., Riquelme, S., Geng, J., Bravo, F., Baez, J. C., et al. (2016). Local tsunami warnings: Perspectives from recent large events. *Geophysical Research Letters*, 43, 1109–1117. <https://doi.org/10.1002/2015GL067100>
- Melgar, D., & Bock, Y. (2013). Near-field tsunami models with rapid earthquake source inversions from land- and ocean-based observations: The potential for forecast and warning. *Journal of Geophysical Research: Solid Earth*, 118, 5939–5955. <https://doi.org/10.1002/2013JB010506>
- Melgar, D., Crowell, B. W., Bock, Y., & Haase, J. S. (2013). Rapid modeling of the 2011  $M_W$  9.0 Tohoku-oki earthquake with seismogeodesy. *Geophysical Research Letters*, 40, 2963–2968. <https://doi.org/10.1002/grl.50590>
- Melgar, D., Crowell, B. W., Geng, J., Allen, R. M., Bock, Y., Riquelme, S., et al. (2015). Earthquake magnitude calculation without saturation from the scaling of peak ground displacement. *Geophysical Research Letters*, 42, 5197–5205. <https://doi.org/10.1002/2015GL064278>
- Miyazaki, S., Larson, K. M., Choi, K., Hikima, K., Koketsu, K., Bodin, P., et al. (2004). Modeling the rupture process of the 2003 September 25 Tokachi-oki (Hokkaido) earthquake using 1-Hz GPS data. *Geophysical Research Letters*, 31, L21603. <https://doi.org/10.1029/2004GL021457>
- Newman, A. V., & Okal, E. A. (1998). Teleseismic estimates of radiated seismic energy: The  $E/M_0$  discriminant for tsunami earthquakes. *Journal of Geophysical Research*, 103, 26,885–26,898. <https://doi.org/10.1029/98JB02236>
- Qian, Y., Wei, S., Wu, W., Zeng, H., Coudurier-Curveur, A., & Ni, S. (2019). Teleseismic waveform complexities caused by near trench structures and their impacts on earthquake source study: Application to the 2015 Illapel aftershocks (Central Chile). *Journal of Geophysical Research: Solid Earth*, 124, 870–889. <https://doi.org/10.1029/2018JB016143>
- Ranero, C. R., & von Huene, R. (2000). Subduction erosion along the Middle America convergent margin. *Nature*, 404(6779), 748–752.
- Regnier, M., Calmant, S., Pelletier, B., & Lagabrielle, Y. (2003). The  $M_W$  7.5 1995 Ambrym earthquake, Vanuatu: A back arc intraplate thrust event. *Tectonics*, 22(4), 1034. <https://doi.org/10.1029/2002TC001422>
- Richter, C. F. (1958). *Elementary seismology* (p. 768). San Francisco: W. H. Freeman and Cooper.
- Sahakian, V. J., Melgar, D., & Muzli, M. (2019). Weak near-field behavior of a tsunami earthquake: Toward real-time identification for local warning. *Geophysical Research Letters*, 46, 9519–9528. <https://doi.org/10.1029/2019GL083989>
- Sathiakumar, S., Barbot, S., Hill, E., Peng, D., Zerucha, J., Suhaimee, S., et al. (2016). Seafloor geodesy using wave gliders to study earthquake and tsunami hazards at subduction zones. *American Geophysical Union, Fall Meeting 2016*, abstract #G31A-1046.
- Scholl, D., & von Huene, R. (2009). Implications of estimated magmatic additions and recycling losses at the subduction zones of accretionary (non-collisional) and collisional (suturing) orogens. *Geological Society, London, Special Publications*, 318(1), 105–125. <https://doi.org/10.1144/SP318.4>
- Shearer, P., & Bürgmann, R. (2010). Lessons learned from the 2004 Sumatra-Andaman megathrust rupture. *Annual Review of Earth and Planetary Sciences*, 38(1), 103–131. <https://doi.org/10.1146/annurev-earth-040809-152537>
- Sladen, A., & Trevisan, J. (2018). Shallow megathrust earthquake ruptures betrayed by their outer-trench aftershocks signature. *Earth and Planetary Science Letters*, 483, 105–113. <https://doi.org/10.1016/j.epsl.2017.12.006>
- Sun, T., Wang, K., Fujiwara, T., Kodaira, S., & He, J. (2017). Large fault slip peaking at trench in the 2011 Tohoku-oki earthquake. *Nature Communications*, 8(1), 14044. <https://doi.org/10.1038/ncomms14044>
- Synolakis, C. E., Bardet, J.-P., Borrero, J. C., Davies, H. L., Okal, E. A., Silver, E. A., et al. (2002). The slump origin of the 1998 Papua New Guinea tsunami. *Proceedings of the Royal Society of London A*, 458(2020), 763–789. <http://doi.org/10.1098/rspa.2001.0915>
- Tanioka, Y. (2018). Tsunami simulation method assimilating ocean bottom pressure data near a tsunami source region. *Pure and Applied Geophysics*, 175(2), 721–729. <https://doi.org/10.1007/s00024-017-1697-5>
- Tappin, D. R., Watts, P., & Grilli, S. T. (2008). The Papua New Guinea tsunami of 17 July 1998: Anatomy of a catastrophic event. *Natural Hazards and Earth System Sciences*, 8(2), 243–266. <https://doi.org/10.5194/nhess-8-243-2008>
- UNDAC. UN Office for the Coordination of Humanitarian Affairs (2000). UNDAC team mission report Bengkulu earthquake, Sumatra, Indonesia 6-16 Jun 2000, <https://reliefweb.int/report/indonesia/undac-team-mission-report-bengkulu-earthquake-sumatra-indonesia-6-16-jun-2000>
- Wang, D., Becker, N. C., Walsh, D., Fryer, G. J., Weinstein, S. A., McCreery, C. S., et al. (2012). Real-time forecasting of the April 11, 2012 Sumatra tsunami. *Geophysical Research Letters*, 39, L19601. <https://doi.org/10.1029/2012GL053081>
- Ward, S. N. (1979). Ringing  $P$  waves and submarine faulting. *Journal of Geophysical Research*, 84(B6), 3057–3062. <https://doi.org/10.1029/JB084iB06p03057>
- Wetzler, N., Lay, T., Brodsky, E. E., & Kanamori, H. (2017). Rupture-depth-varying seismicity patterns for major and great ( $M_W \geq 7.0$ ) megathrust earthquakes. *Geophysical Research Letters*, 44, 9663–9671. <https://doi.org/10.1002/2017GL074573>
- Wiens, D. A. (1987). Effects of near source bathymetry on teleseismic  $P$  waveforms. *Geophysical Research Letters*, 14(7), 761–764. <https://doi.org/10.1029/GL014i007p00761>
- Wiens, D. A. (1989). Bathymetric effects on body waveforms from shallow subduction zone earthquakes and application to seismic processes in the Kurile trench. *Journal of Geophysical Research*, 94(B3), 2955–2972. <https://doi.org/10.1029/JG094iB03p02955>

- Wright, T. J., Houlié, N., Hildyard, M., & Iwabuchi, T. (2012). Real-time, reliable magnitudes for large earthquakes from 1 Hz GPS precise point positioning: The 2011 Tohoku-oki (Japan) earthquake. *Geophysical Research Letters*, *39*, L12302. <https://doi.org/10.1029/2012GL051894>
- Wu, W., Ni, S., Zhan, Z., & Wei, S. (2018). A SEM-DSM three-dimensional hybrid method for modeling teleseismic waves with complicated source-side structures. *Geophysical Journal International*, *215*(1), 133–154. <https://doi.org/10.1093/gji/ggy273>
- Yamazaki, Y., Cheung, K. F., & Lay, T. (2018). A self-consistent fault slip model for the 2011 Tohoku earthquake and tsunami. *Journal of Geophysical Research: Solid Earth*, *123*, 1435–1458. <https://doi.org/10.1002/2017JB014749>
- Yamazaki, Y., Cheung, K. F., Pawlak, G., & Lay, T. (2012). Surges along the Honolulu coast from the 2011 Tohoku tsunami. *Geophysical Research Letters*, *39*, L09604. <https://doi.org/10.1029/2012GL051624>
- Ye, L., Lay, T., & Kanamori, H. (2013). Ground shaking and seismic source spectra for large earthquakes around the megathrust fault offshore of northeastern Honshu, Japan. *Bulletin of the Seismological Society of America*, *103*(2B), 1221–1241. <https://doi.org/10.1785/0120120115>
- Ye, L., Lay, T., Kanamori, H., & Rivera, L. (2016). Rupture characteristics of major and great ( $M_W \geq 7.0$ ) megathrust earthquakes from 1990 to 2015: 1. Source parameter scaling relationships. *Journal of Geophysical Research: Solid Earth*, *121*, 826–844. <https://doi.org/10.1002/2015JB012426>
- Yue, H., Castellanos, J. C., Yu, C., Meng, L., & Zhan, Z. (2017). Localized water reverberation phases and its impact on backprojection images. *Geophysical Research Letters*, *44*, 9573–9580. <https://doi.org/10.1002/2017GL073254>
- Yue, H., Lay, T., Rivera, L., An, C., Vigny, C., Tong, X., & Báez Soto, J. C. (2014). Localized fault slip to the trench in the 2010 Maule, Chile  $M_W$  8.8 earthquake from joint inversion of high-rate GPS, teleseismic body waves, InSAR, campaign GPS, and tsunami observations. *Journal of Geophysical Research: Solid Earth*, *119*, 7786–7804. <https://doi.org/10.1002/2014JB011340>